

# Evolution of dwarf early-type galaxies I. Spatially resolved stellar populations and internal kinematics of Virgo cluster dE/dS0 galaxies.

Igor V. Chilingarian<sup>1,2?</sup>

<sup>1</sup>Observatoire de Paris-Meudon, LERMA, UMR 8112, 61 Av. de l'Observatoire, 75014 Paris, France

<sup>2</sup>Sternberg Astronomical Institute, Moscow State University, 13 Universitetsky prospect, 119992, Moscow, Russia

Accepted 2008 Dec 17. Received 2008 Dec 10; in original form 2008 Oct 16

## ABSTRACT

Understanding the origin and evolution of dwarf early-type galaxies remains an important open issue in modern astrophysics. Internal kinematics of a galaxy contains signatures of violent phenomena which may have occurred, e.g. mergers or tidal interactions, while stellar population keeps a fossil record of the star formation history, therefore studying connection between them becomes crucial for understanding galaxy evolution. Here, in the first paper of the series, we present the data on spatially resolved stellar populations and internal kinematics for a large sample of dwarf elliptical (dE) and lenticular (dS0) galaxies in the Virgo cluster. We obtained radial velocities, velocity dispersions, stellar ages and metallicities out to 1/2 half-light radii by re-analysing already published long-slit and integral-field spectroscopic datasets using the NBURSTS full spectral fitting technique. Surprisingly, bright representatives of the dE/dS0 class ( $M_B = -18.0 \pm 0.1$  mag) look very similar to intermediate-mass and giant lenticulars and ellipticals: (1) their nuclear regions often harbour young metal-rich stellar populations always associated with the drops in the velocity dispersion profiles; (2) metallicity gradients in the main discs/spheroids vary significantly from nearly flat profiles to  $-0.9 \text{ dex } r_e^{-1}$ , i.e. somewhat 3 times steeper than for typical bulges; (3) kinematically decoupled cores were discovered in 4 galaxies, including two with very little, if any, large scale rotation. These results suggest similarities in the evolutionary paths of dwarf and giant early-type galaxies and call for reconsidering the role of major mergers in the dE/dS0 evolution.

**Key words:** galaxies: dwarf { galaxies: elliptical and lenticular, cD { galaxies: evolution { galaxies: stellar content { galaxies: kinematics and dynamics

## 1 INTRODUCTION

Dwarf elliptical (dE) and lenticular (dS0) galaxies, low-luminosity ( $M_B > -18.0$  mag) stellar systems with early-type morphology, represent the numerically dominant galaxy population in nearby galaxy clusters and groups (Ferguson & Binggeli 1994). In the cold dark matter models of hierarchical galaxy formation they are considered as the building blocks of presently observed stellar systems (e.g. White & Frenk 1991). Thus, understanding their formation and evolution becomes one of the important questions of modern astrophysics. Several dE/dS0 formation scenarios were proposed (see review and discussion in De Rijcke et al. 2005), but none of them is able to fully explain all observa-

tional properties of these galaxies simultaneously. A possible diversity of evolutionary scenarios has been suggested by van Zee et al. (2004a) and later investigated by Lisker et al. (2008) to explain properties of different dE subclasses, although Boselli et al. (2008a) insist on the ram pressure stripping to be the unique channel of dE formation.

Dwarf and giant early-type galaxies form two distinct sequences in the absolute magnitude ( $M_B$ ) vs effective surface brightness ( $\mu_e$ ) diagram (see e.g. Ferguson & Binggeli 1994) joining around  $M_B = -18.0$  mag, which is often referred as a luminosity separating these two classes (see Boselli et al. 2008b and Komendy et al. 2008 for the recent discussions). Although, some arguments are provided (e.g. Graham & Guzman 2003) for the continuity of the dwarf/giant sequence on the  $M_B$  vs  $\mu_e$  plot, it is clear that the effective surface brightness of dE galaxies correlates with

? E-mail: Igor.Chilingarian@obspm.fr

their luminosity, or, in other words, less luminous galaxies are fainter in terms of surface brightness, making their observations a challenging task. One has to keep in mind that dE galaxies usually lack of the interstellar medium (ISM), therefore their spectra normally contain no emission lines. This explains why the first kinematical study of dEs (Bender & Nieto 1990) appeared more than a decade after the publication of the absorption-line kinematics of giant elliptical galaxies (e.g. Bertola & Capaccioli 1975).

New debates addressing the dE formation appeared recently: Boselli et al. (2008a,b) argue for the ram pressure stripping to be the only scenario of dE formation, hence making these galaxies evolutionary different from giant early-type systems and reproducing their locus on the  $M_B$  vs  $h_{16}$  plot; while Janz & Lisker (2008) succeeded to explain the observed discontinuity of giant and dwarf ellipticals in the size(luminosity) relation by comparing a large homogeneous imaging dataset to the predictions of semi-analytical models of elliptical galaxy formation, thus suggesting their common origin. Comparing the structural properties of dwarf galaxies to their internal kinematics and stellar populations therefore becomes a question of major importance for understanding dE/dS0 formation and evolution.

The significant progress in the astronomical instrumentation and new detectors having low readout noise became the cornerstones to the accomplishments of several projects assessing spatially-resolved kinematics of diffuse elliptical galaxies in different environmental conditions. Kinematical profiles presented in Derijcke et al. (2001, 2003); Geha et al. (2002, 2003); Pedraz et al. (2002); Simien & Prugniel (2002); van Zee et al. (2004b) revealed a diversity of the degree of rotational support and presence of kinematically-decoupled components in some objects (Derijcke et al. 2004; Geha et al. 2005; Prugniel et al. 2005; Thomas et al. 2006). Detailed studies of the morphological properties of dEs revealed embedded structures such as stellar discs, sometimes harbouring low-contrast spiral arms, or bars in many galaxies (Jerjen et al. 2000; Barazza et al. 2002; Lisker et al. 2006). These discoveries strengthen the evolutionary connection between dwarf ellipticals and discy late-type dwarfs.

At the same time, studies of the stellar population properties of dwarf elliptical galaxies still remain a challenge both for observations and for the data analysis, because absorption line strengths, a traditional spectroscopic indicator of stellar populations (see e.g. Worthey et al. 1994 for the description of the Lick system) require high signal-to-noise ratios in order to reach reasonable quality of age and metallicity estimates. Some attempts were made to derive dE stellar populations from the narrow-band photometry (Rakos et al. 2001). However, the calibrations used by the authors were based on Galactic globular clusters, therefore an assumption about very old ages was done, resulting in low metallicity estimates ( $-1.4$  to  $-0.6$  dex). The integrated measurements of dE stellar populations from the Lick indices were made later (Geha et al. 2003; van Zee et al. 2004a) and revealed populations having intermediate ages of  $3\text{--}5$  Gyr, and considerably higher metallicities around  $-0.5$  dex. These results were confirmed and extended to a larger sample of Virgo cluster dEs recently (Michielsen et al. 2008).

A new family of techniques for recovering stellar

population properties from integrated light spectra appeared recently (Cid Fernandes et al. 2005; Ocvirk et al. 2006; Chilingarian et al. 2007c). These methods are based on the fitting of the stellar population models against the observed spectra in the pixel space. Since every pixel of an absorption-line galactic spectrum bears information about the stellar content of a galaxy, these techniques are potentially much more sensitive than the line-strength indices dealing with the individual spectral features. Another advantage of the pixel space fitting is an easy way of getting rid of residual cosmic ray hits and regions of the spectra contaminated by emission lines by excluding these regions from the fitting procedure.

The full spectral fitting using the NBursts code (see preliminary description in Chilingarian 2006; Chilingarian et al. 2007b) allowing to extract internal kinematics simultaneously with the parametrized star formation history, was successfully used in the studies of integrated kinematical and stellar population properties of dE galaxies in the Fornax (Michielsen et al. 2007) and Abell 496 (Chilingarian et al. 2008c) clusters. The method was shown to be stable and working well even for the data having low signal-to-noise ratios.

Up to now, a published sample of dwarf and low-luminosity early-type galaxies with the spatially-resolved stellar population information (apart from Local Group dwarfs studied by means of colour-magnitude diagrams) contains only seven objects, all of them observed with the Multi-Pupil Field Spectrograph (Afanasyev et al. 2001) at the 6-m Bolshoi Teleskop Altazimutal'nij (BTA) of the Special Astrophysical Observatory of the Russian Academy of Sciences (SAO RAS). The sample includes four dE/dS0s in the Virgo cluster (Chilingarian et al. 2007c,d) and three low-luminosity E/S0s in groups: NGC 770 (Prugniel et al. 2005), NGC 126 and NGC 130 (Chilingarian et al. 2008b). In all cases the two-dimensional maps of kinematics and stellar population properties were obtained using the NBursts technique. Chemically and evolutionarily decoupled structures which are quite common in giant elliptical and lenticular galaxies (Sil'chenko 2006; Kuntschner et al. 2006) were detected in the central regions of six low-luminosity galaxies.

Presently, the growing amount of high-quality optical spectroscopic data on dwarf galaxies becomes available in the archives of major observatories. Therefore, we decided to re-analyse the existing and available spectroscopic data for dE/dS0 galaxies using the full spectral fitting technique. The project aims at studying the connection between internal kinematics and stellar populations of dE galaxies and understanding the mechanisms of their formation and evolution, primarily in the cluster environment.

In the first paper of the series we provide the kinematical and stellar population profiles of Virgo cluster dE/dS0 galaxies obtained from the new analysis of several published datasets carried out using the NBursts full spectral fitting technique (Chilingarian et al. 2007b,c). The thorough discussion of the obtained results will be given in the next papers. The paper is organized as follows: in Section 2 we describe the spectroscopic data, data reduction procedures, and define a sample of galaxies, Section 3 provides details about the techniques used to analyse the data, Section 4 presents the results of this analysis, the conclusions are given in Section 5.

## 2 THE DATA AND THE SAMPLE

In the course of our study we have used intermediate-resolution ground-based spectroscopic data coming from various sources. The criteria we applied to select the datasets were: (1) only published data with available advanced calibrations such as stellar templates, twilight spectra, or well-defined spectral resolution information and well-documented spectrograph; (2) coverage of the blue/green spectral region ( $4800\text{\AA} < \lambda < 5400\text{\AA}$ ) containing prominent absorption features; (3) intermediate spectral resolution not lower than  $R = 1300$  to be able to constrain kinematics simultaneously with stellar populations and tackle the degeneracy between metallicity and velocity dispersion; (4) we gave preference to the data having intermediate or high signal-to-noise ratio and spatially resolved datasets (i.e. longslit or IFU spectroscopy). Hereafter we present the data collections used in order of their importance for our study and briefly discuss essential data reduction steps which had to be considered prior to the analysis.

### 2.1 Palomar dE Project: Long-Slit Spectroscopy

Observations of 16 Virgo Cluster dwarf and low-luminosity early-type galaxies were conducted with the Double Spectrograph at the 5-m Palomar telescope during two observing runs in March 2001 and April 2002. The reduced, sky-subtracted, flux-calibrated datasets were kindly provided by L. Van Zee (PI of the project) in fall 2004. The two wavelength ranges were observed with the double beam spectrograph:  $4800\{5700\text{\AA}$  with the resolving power  $R \approx 2200$ , and  $8250\{8900\text{\AA}$  having higher spectral resolution ( $R \approx 5400$ ). Integration times ranged from 1200 sec for VCC 1075 to 12000 sec for VCC 1308. The 2 arcsec wide slit spanned 2 arcmin and was placed along major axes of the observed galaxies (see Table 2 in van Zee et al. 2004b). A number of radial velocity standards (F7{K2 giants) was observed.

We refer to all the details regarding observations and data reduction to van Zee et al. (2004b), where thorough kinematical analysis of these data is presented. In this study we make a direct use only of the blue beam spectra centered on the Mgb triplet; the red beam kinematics from van Zee et al. (2004b) is used for comparison with the kinematical profiles we obtain.

We used the spectra of HD 136202, HD 182572, and HD 187691 obtained with the same instrument in March and September 2001 and provided to us together with the spectra of galaxies, to compute the variations of the spectral line spread function (LSF) along the wavelength and assess the precision of the data reduction. The analysis of the 10 spectra of HD 182572 obtained for different positions of the star on the slit allowed us to assess the spatial variations of the spectral resolution.

We fit the stellar spectra against the high-resolution spectra of the corresponding stars available in the ELODIE 3.1 (Pruget et al. 2007) library in five wavelength segments covering the spectral range of the blue setup of the Double Spectrograph and overlapping by 20 per cent. The fitting was done using the penalized pixel fitting procedure (Cappellari & Emsellem 2004) returning  $v$ ,  $\sigma$ ,  $h_3$ , and  $h_4$  coefficients of the Gauss-Hermite parametrization (van der Marel & Franx 1993). The heliocentric radial ve-

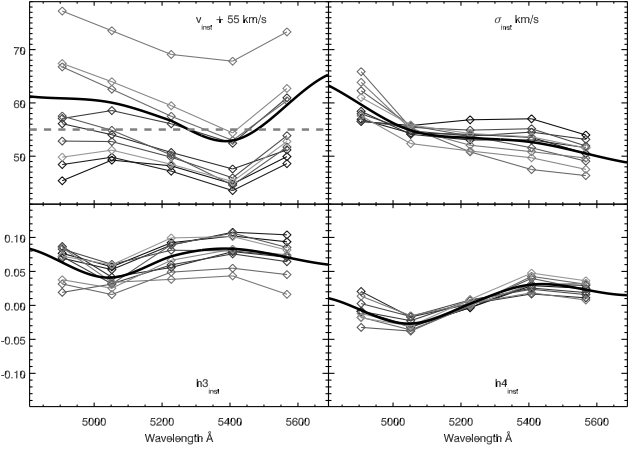


Figure 1. Wavelength-dependent variations of the Gauss-Hermite parametrization coefficients of the Double Spectrograph LSF at the Palomar 5-m Hale Telescope obtained from the fitting of the 10 HD 182572 spectra. The adopted curves are displayed by solid bold lines.

locities available from the ELODIE 3.1 library have been subtracted from the fitting results. Then the heliocentric corrections were computed for every individual spectrum using the `iraf.noao.rv.rvcorrect` task and applied to the measurements.

In case of perfect and unbiased wavelength calibration this procedure would result in zero radial velocities, while non-zero values would measure the systematic errors of the dispersion relation. Variations of  $\sigma$ ,  $h_3$ , and  $h_4$  along the wavelength are caused by the distortions introduced by the optical system of the spectrograph both, in the collimator and in the camera. The mean value of the  $h_4$  coefficient anti-correlates with the slit width: wider slit resulting in the  $\lambda$ -shaped line profile corresponds to negative  $h_4$ , as in e.g. VLT FLAMES/Giraffe (Chilingarian et al. 2008c), where the physical diameters of optical fibers are larger than the diffraction limit of the collimator.

In Fig 1 we present the variations of the Gauss-Hermite parametrization coefficients along the wavelength obtained from the fitting of 10 individual spectra of HD 182572. The adopted behaviour of the coefficients which we use to transform the PEGASE HR models into the resolution of the Double Spectrograph are shown by solid bold lines.

The measurements for individual spectra are scattered between  $-10$  and  $30 \text{ km s}^{-1}$ , which is probably caused by the excursions in the instrument resulting in the overall shift of the wavelength solution zero-point. Therefore, we can expect systematic errors of the radial velocity measurements of an order of  $20 \text{ km s}^{-1}$ . However, since our study is not aimed at the accurate measurements of absolute radial velocities of galaxies, this effect is not critical for us and affects none of our scientific conclusions. We did not notice any correlation between the measured systematic radial velocity offset and the position of the star on the slit. Good agreement of the radial velocity profiles for some objects with different datasets (see below) also suggests no important systematic errors of the wavelength solution along the slit.

We also see an overall trend along the wavelength range, which is very well reproduced by the measurements made on

all individual spectra: the systematic values first smoothly decrease by  $7 \text{ km s}^{-1}$  between 4800 and 5400 Å, and then increase by  $8 \text{ km s}^{-1}$  to the red end of the wavelength range. This behaviour may be a result of an insufficient order of the polynomial used to approximate the wavelength solution during the data reduction procedure.

The spectral resolution ( $\lambda_{\text{inst}}$ ) as a function of wavelength (Fig 1) rapidly rises from  $65$  to  $55 \text{ km s}^{-1}$  between 4800 and 5050 Å then slowly increasing to  $48 \text{ km s}^{-1}$  at 5650 Å. This behaviour keeps very similar for all the analysed spectra, suggesting no important variations of the spectral resolution along the slit.

Within the precision of the measurements ( $0.03$ ), the  $h_3$  coefficient remains stable along the wavelength range with the mean value of  $+0.05$ , suggesting slight overall asymmetry of the DS blue arm LSF. The  $h_4$  coefficient also demonstrates very stable behaviour for different wavelength with the mean value of  $0.00$  with a smooth gradient from  $-0.03$  to  $+0.03$ , which is the same order as the uncertainties of the measurements.

Hence, the overall variations of the Double Spectrograph LSF in the blue beam exhibit very reproducible behaviour along the wavelength showing neither significant changes along the slit, nor time-dependent drifts. The wavelength dependent variations of the spectral resolution and radial velocity systematics are taken into account while fitting the spectra of galaxies by convolving the PEGASE-HR stellar population models using the wavelength-dependent kernel, as described in Section 4.1 of Chilingarian et al. (2007c). Briefly, several (usually, five) sets of models are created by convolving the original grid with LSF for different (five) positions along the wavelength, then the linear interpolation between these sets is done at every wavelength. This allows to obtain trustworthy velocity dispersion measurements down to  $1/3$  of the instrumental resolution (i.e.,  $20 \text{ km s}^{-1}$ ) at intermediate signal-to-noise ratios ( $> 20$ ) which is very important for reliable estimations of the stellar population parameters (Chilingarian et al. 2008a).

The initial sample of van Zee et al. (2004b) included two galaxies having poor signal-to-noise ratios: VCC 1743 and VCC 1857. For these objects we provide only integrated measurements of kinematics and stellar populations along the slit. For the other 14 objects we have performed the adaptive binning along the slit in order to reach the minimal signal-to-noise ratio of 20 or 30 (10 for VCC 1075) per individual bin per pixel at 5200 Å. This was done by co-adding individual consequent pixels along the slit from the centre towards outer regions of the galaxy until the target signal-to-noise ratio had been reached. The first bin was always assigned to the photometric galaxy centre on the slit and grown in both directions. For the kinematic and stellar population analysis the data have been rebinned logarithmically in wavelength with the step corresponding to  $40 \text{ km s}^{-1}$ .

## 2.2 HyperLeda FITS Archive: Long-Slit Spectroscopy

The HyperLeda project<sup>1</sup> (Paturel et al. 2003) known mostly by its largest existing database of homogenised structural, photometric, and kinematical parameters of galaxies, also contains a rich collection of raw and processed spectral and imaging datasets known as the HyperLeda FITS Archive (HFA). This resource includes all the data on early-type galaxies presented in a series of papers by Simien & Prugniel originating from the CARELEC long-slit spectrograph at the 1.93 m telescope of l'Observatoire de Haute-Provence. In our study we use the subset of this collection devoted to dwarf and low-luminosity early-type galaxies in the Virgo cluster and presented in detail in Simien & Prugniel (2002). The data were obtained during 5 observing runs in April and June, 1999, February and March, 2000, and January, 2001. The CARELEC setup # 2 provided intermediate spectral resolution of  $R \approx 5000$  at the wavelength range  $4700 < \lambda < 5600$  Å for the 5 arm in long slit. The slit widths as specified in the metadata (FITS headers) were: 2.2, 2.1, 2.3, 1.8, and 1.7 arcsec for the five observing runs mentioned above. The integration times ranged from 60 minutes in a single exposure for NGC 4476 to 210 minutes in four exposures for IC 3461. The complete observing log is available in Table 2 of Simien & Prugniel (2002).

We used the original raw CCD frames available in the archive and reduced them using our software package originally developed for the IFU data reduction and adapted to the long-slit spectroscopy. The main steps of the data reduction include: (1) subtraction of bias; (2) cleaning cosmic ray hits using Laplacian filtering (van Dokkum 2001) (3) preliminary flat-field correction using dome flat; (4) automatic identification of the arc line spectrum (He, Ne, Ar) and building the wavelength solution using the 3<sup>rd</sup> order polynomial; (5) rebinning the spectra logarithmically in wavelength with the step of  $25 \text{ km s}^{-1}$ ; (6) residual flat-field correction using twilight frames. In average, 30 arc lines were used to build the wavelength solution, resulting in the accuracy of about  $0.04 \text{ Å}$ .

For all the observing runs, but April 1999, we used the twilight spectra obtained in the same observing mode of the instrument in order to assess variations of the CARELEC LSF along the wavelength range and along the slit. We fit them against a high-resolution spectrum of the Sun available in the ELODIE 3.1 spectral library exactly the same way as the stellar spectra from the Palomar DE project. The LSF was shown not to exhibit any changes along the slit. At the same time there are modest variations along the wavelength range: the radial velocity systematic offset and  $\lambda_{\text{inst}}$  (in parenthesis) change smoothly from  $+2$  (32 to 50 for different observing runs) in the blue to  $-2$  (25 to 40)  $\text{km s}^{-1}$  in the red end of the wavelength range;  $h_3$  stays within 0.01 from zero;  $h_4$  decreases from  $+0.04$  to  $0.00$ .

There are important changes of the instrumental resolution  $\lambda_{\text{inst}}$  between the observing runs because of different slit widths used. No twilight spectra were obtained in the April 1999 observing run, however, two stars included in the ELODIE 3.1 library were observed: HD 84937

<sup>1</sup> <http://leda.univ-lyon1.fr/>



and HD 137759. The former is a relatively early type star (F5 III), therefore its spectrum does not contain sufficient amount of deep spectral lines to measure accurately the spectral resolution variations. However, the latter one, a K-type giant, has an appropriate spectrum to determine the spectrograph's LSF.

We did not use the data for four galaxies, IC 3120, IC 3457, IC 3653, and NGC 4482. IC 3120 is a late-type dwarf and is out of the scope of this study; IC 3653 was observed under very poor atmosphere conditions (6 arcsec seeing); and the two remaining objects have too low signal (perhaps due to poor transparency for NGC 4482) to determine stellar population parameters. We notice that the data for IC 3457 also contain the spectrum of PGC 41516 (VCC 1399) on the slit, but it is also too faint even for integrated measurements of stellar populations.

Finally, we used the data for 15 galaxies, 3 of those also having the data available from the Palomar dE project. Spectra of some objects (e.g. IC 783A) have poor signal-to-noise ratios, therefore we provide only integrated measurements of the stellar population parameters along the slit. For the remaining galaxies we performed the adaptive binning along the slit to reach them in minimal signal-to-noise ratio of 10 or 15 per bin per pixel at 5200Å using the technique described in the previous subsection.

### 2.3 IFU Spectroscopy of Four dE Galaxies

Four bright dE/dS0 galaxies, IC 783, IC 3468, IC 3509, and IC 3653 were observed using the MPFS IFU spectrograph at the Russian 6-m telescope BTA SAO RAS during 3 observing runs in March 2004, May 2004, and May 2005. The details about observations, data reduction and analysis were presented in Chilingarian (2006) and Chilingarian et al. (2007c,d). All the data are available in the ASPID archive (Chilingarian et al. 2007a).

Here we include the original measurements presented the corresponding papers for two galaxies, VCC 490 and VCC 1871. We re-analysed the data for another two objects, VCC 1422 and VCC 1545, improving the sky subtraction and increasing the power of the multiplicative polynomial continuum to 15 (see next section). The data were spatially rebinned using the Voronoi adaptive binning technique (Cappellari & Copin 2003) to reach minimal target signal-to-noise ratio per bin.

### 2.4 SDSS DR6: Aperture Spectroscopy

The Virgo cluster is partially contained in the footprint of the Sloan Digital Sky Survey Data Release 6 (Adelman-McCarthy et al. 2008). Therefore, relatively high signal-to-noise ratio flux calibrated intermediate-resolution ( $R \approx 1800$ ) spectra covering a large wavelength range ( $3800 < \lambda < 9200\text{Å}$ ) are available for many dE/dS0 cluster members. We use SDSS spectra for the objects from the samples presented above in order to compare the stellar population properties in the inner regions of the galaxies. Relatively low spectral resolution of the data did not allow us to measure velocity dispersions below  $40 \text{ km s}^{-1}$ .

The spectra were obtained using the 2.5 m Apache Point Observatory telescope with the multi-object double spectrograph containing 640 3-arcsec wide circular fibres in the

3 deg<sup>2</sup> field of view (Gunn et al. 2006). The spectroscopic target selection of SDSS is based on the limiting magnitude inside the fibre aperture, therefore the sample is biased towards nucleated dwarf galaxies.

Since neither twilight spectra were available in the SDSS archive, nor bright stars included in the ELODIE 3.1 library were targeted by the SDSS due to high fluxes, it is not possible to directly measure the LSF variations of the SDSS spectrograph along the wavelength. However, the changes of the spectral resolution in terms of  $\lambda_{\text{inst}}$  are computed for each fibre by the SDSS data processing pipeline and provided together with the data (in the 5<sup>th</sup> extension of FITS files containing extracted spectra).  $\lambda_{\text{inst}}$  decreases from  $68 \text{ km s}^{-1}$  at 3800Å to  $52 \text{ km s}^{-1}$  at 5800Å. Then it sharply jumps to  $66 \text{ km s}^{-1}$  smoothly decreasing down to  $51 \text{ km s}^{-1}$  at 9200Å. This happens because SDSS spectra include two parts (blue and red) obtained in the two different arms of the instrument. Here we treat the SDSS spectra in the wavelength range between  $3900 < \lambda < 6700\text{Å}$  (rest-frame). In addition to a wide coverage of the spectral domain resulting in better quality of the stellar population parameter estimates by the full spectral fitting, the centre of the selected wavelength interval, 5300Å, well corresponds to the discussed long-slit spectroscopic data.

23 of 31 galaxies included in our final sample have SDSS DR6 spectra available.

Our final sample is presented in Table 1. We provide the common galaxy designations, their numbers in the Virgo Cluster Catalogue (Binggeli et al. 1985) and availability of data in every of the discussed datasets. The sample spans a range of luminosities  $18.27 < M_B < 15.10 \text{ mag}$ , central velocity dispersions  $23 < \sigma < 79 \text{ km s}^{-1}$ . It is not a statistically representative sample of the Virgo cluster dE galaxies, because of the well-known correlation of the luminosity and effective surface brightness of dE/dS0s, making fainter galaxies (in terms of the luminosity) more difficult to observe. For several objects among the least luminous members of our sample we provide only integrated measurements of the stellar populations properties. The faintest object with the spatially resolved information available is VCC 1308 ( $M_B = 15.41 \text{ mag}$ ).

## 3 DATA PROCESSING AND ANALYSIS

We have treated the high-resolution pegaséhr (Le Borgne et al. 2004) simple stellar population (SSP) models against the observational data using the NBursts full spectral fitting technique (Chilingarian et al. 2007c,b). We computed the SSP models for the Salpeter (1955) stellar initial mass function using the recent version of the ELODIE stellar library (v 3.1, Pignatelli et al. 2007) providing a spectral resolution of  $R = 10000$  in the wavelength range  $3900 < \lambda < 6800\text{Å}$ .

The spectral fitting method is based on the non-linear least square fitting using the constrained Levenberg-Marquardt optimisation of the following quantity:

$$\chi^2 = \sum_N \frac{(F_i - P_{1p}(T_i(\text{SFH})) - L(v_i; h_3; h_4) + P_{2q})^2}{F_i^2};$$

where  $T_i(\text{SFH}) = \sum_{N_{\text{bursts}}} k_i T_i(t_n; Z_n)$  (1)

Table 1. Final sample of low-luminosity dwarf early-type galaxies in the Virgo cluster. Columns (1) and (2) give the object name and VCC number, columns (3)–(5) indicate availability of the data, column (6) provides the source of photometric data. Galaxies observed with the MPFS IFU spectrograph are shown in *italic*.

Name	VCC	Pal.	OHP	SDSS	Ph.ref
IC 3081	178	yes	no	yes	3
IC 781	389	no	yes	yes	4
UGC 7399A	437	yes	no	no	1
IC 783	490	no	yes <sup>1</sup>	yes	4
UGC 7436	543	yes	yes	yes	1
IC 783A	545	no	yes <sup>1</sup>	yes	4
NGC 4328	634	no	yes	yes	4
IC 3328	856	no	yes	yes	1
IC 3344	917	yes	no	yes	2,3
IC 3363	965	yes	no	yes	3
IC 3369	990	yes	no	yes	3
NGC 4431	1010	no	yes	no	4
NGC 4436	1036	yes	yes	yes	2,3
IC 3383	1075	yes	no	yes	1
IC 3381	1087	no	yes	yes	1
IC 3393	1122	yes	yes	yes	3
IC 3413	1183	no	yes	no	4
NGC 4476	1250	no	yes	yes	1
NGC 4482	1261	yes	no <sup>2</sup>	yes	1
IC 3437	1308	yes	no	no	3
IC 3461	1407	no	yes <sup>1</sup>	yes	1
IC 3468	1422	no	no	yes	1
IC 3486	1491	no	yes	yes	4
PGC 41726	1514	yes	no	no	3
IC 3509	1545	no	no	yes	1
IC 3602	1743	yes <sup>1</sup>	no	yes	1
IC 3647	1857	yes <sup>1</sup>	no	no	1
IC 3653	1871	no	no <sup>3</sup>	yes	1
IC 3735	2019	yes	no	no	1
IC 3773	2048	no	yes	no	1
IC 3779	2050	yes	no	yes	1

<sup>1</sup> poor signal-to-noise ratio, only integrated measurements are possible

<sup>2</sup> very poor signal-to-noise ratio, object excluded

<sup>3</sup> poor seeing, object excluded

Photometric references: 1 { Ferrarese et al. (2006), 2 { Stiavelliet al. (2001) and/or Geha et al. (2003), 3 { van Zee et al. (2004a), 4 { SDSS DR 6

where  $L$  is the line-of-sight velocity distribution in the Gauss-Hermite parametrization (van der Marel & Franx 1993);  $F_i$  and  $F_{i\sigma}$  are observed flux and its uncertainty;  $T_i(\text{SFH})$  is the flux from a synthetic spectrum, represented by a linear combination of  $N_{\text{bursts}}$  SSPs and convolved according to the line-spread function of the spectrograph;  $P_{1p}$  and  $P_{2q}$  are multiplicative and additive Legendre polynomials of orders  $p$  and  $q$  for correcting the continuum;  $t_n$  and  $Z_n$  are age and metallicity of the  $n^{\text{th}}$  SSP. The relative contributions of the SSPs and the additive continuum are  $t$  linearly at every evaluation of the function, whereas all the remaining parameters (including  $P_{2q}$  for the additive continuum) are derived from the non-linear optimisation. The needs for multiplicative continuum and possible side-effects have been presented and analysed in detail in Appendix A 2.3 of Chilingarian et al. (2007c), Appendix B 1 of Chilingarian et al. (2008c), and Koleva et al. (2008).

If emission lines present in the spectrum, the wavelength regions contaminated by them are excluded from the fitting. In the wavelength range of SDSS we then exclude Balmer lines (7Å-wide intervals),  $\text{D III} \lambda$  (4363, 4959, 5007 Å),  $\text{N II} \lambda$  (5199 Å),  $\text{N I} \lambda$  (6548, 6583 Å), and  $\text{S II} \lambda$  (6717, 6731 Å). Besides, we always exclude from the fitting the spectral regions contaminated by the strong air-glow lines:  $\text{D I} \lambda$  (5577, 6300, 6364 Å),  $\text{Na I} \lambda$  (5890, 5896 Å), and mercury lines originating from the light pollution, the strongest one being  $\text{Hg I} \lambda$  (5461 Å).

The stellar population properties were derived in the parameter space with the rotated age and metallicity axes as described in Section 3 of Chilingarian et al. (2008c):

$$\begin{aligned} &= (3Z + 2 \log_{10} t)^{\frac{p}{13}}; \\ &= (2Z + 3 \log_{10} t)^{\frac{p}{13}} \end{aligned} \quad (2)$$

In this coordinate system the  $t$  axis is parallel to the direction of the well-known age-metallicity degeneracy for old stellar populations in the age-metallicity space expressed by Worthey (1994) as "if the percentage change  $\Delta \text{age} = Z/3-2$  for two populations, they will appear almost identical in most indices".

All the results presented in this paper correspond to the fitting of a single SSP. We did not include the additive polynomial in the fitting. The adopted values of the multiplicative polynomial continuum were 13, 13, and 15 for the Palomar dE, HFA, and SDSS datasets respectively. In one of the next papers of the series we will present the fitting of the nuclear regions of the galaxies with a more complex model containing two stellar populations.

It was shown by Koleva et al. (2008) that the full spectral fitting using the NBURSTS code produced consistent stellar population parameters with those derived from the measurements of the Lick indices, being several times more precise. Here we also stress that (1) age determinations from the full spectral fitting are insensitive to the masking of Balmer lines (see Appendix A 2 in Chilingarian et al. 2007c and Appendix B in Chilingarian et al. 2008c); (2) velocity dispersions can be precisely determined at down to  $1/3(1/2)$  of the spectral resolution (i.e.  $15(20) \text{ km s}^{-1}$  for the HFA data and  $18(25) \text{ km s}^{-1}$  for the Palomar dE data) and these measurements remain unbiased (see e.g. Koleva et al. 2007 and Section 2 in Chilingarian et al. 2008a); (3) more optimal usage of the information contained in the spectrum by the full spectral fitting compared to the techniques using line-strength indices results in considerably higher precision of the derived stellar population parameters or, reciprocally, lower values of the required signal-to-noise ratio per Å to get the comparable uncertainties (see e.g. Koleva et al. 2007); (4) luminosity-weighted values of ages and metallicities are insensitive to the  $\alpha/\text{Fe}$  ratios of the populations being  $t$  (Chilingarian et al. 2008c; Koleva et al. 2008) even when using the PEGASE HR SSP models not representative of metal-rich  $\alpha$ -enhanced populations since they are based on the empirical stellar library, which contains stars only from the Solar neighbourhood, where  $\alpha/\text{Fe}$  abundance ratios are correlated with their metallicities.

We have conducted a numerical experiment to quantify the age- and metallicity-sensitive information in the absorption-line spectra in order to illustrate the points (1) and (3) mentioned above. Since the flux at every wavelength

contributes to the total value of  $\chi^2$  and this contribution depends on many parameters, a possible way to estimate the sensitivity of the fitting procedure  $S(\lambda; p_0, \dots, p_n)$  to a given parameter  $p_i$  at a given wavelength  $\lambda$  is to compute the corresponding partial derivative of the template grid accounting for the multiplicative continuum variations. In our case the sensitivity to a stellar population parameter (and similarly,  $\sigma$ ) at a point of the parameter space  $(t; Z; \sigma)$  will be expressed as:

$$S(\lambda; t; Z; \sigma) = \frac{\partial}{\partial p_i} \chi^2_{\text{fit}}(\lambda; t; Z; \sigma) \left( \frac{\partial \chi^2_{\text{fit}}}{\partial p_i} \right)^{-1} \quad (3)$$

with the quantities defined in Eq. 1, 2 assuming SFH containing a single SSP. This means, that the squared fitting residuals of a spectrum  $(O + M; \lambda)$  against the model  $(M; \lambda)$  at every pixel would reflect its contribution to the overall  $\chi^2$  when varying  $\lambda$ , i.e. its sensitivity to, or, in other words, the measure of information about a given stellar population parameter.

Practically, the computation is straightforward and has been conducted as follows. We have chosen six PEGASE HR "reference SSPs" representing stellar populations with ages of 1.5, 5, and 12 Gyr and metallicities of -1.0 and -0.3 dex. Then, for every of the six "reference SSPs", six models have been constructed by convolving them with three Gaussians corresponding to the velocity dispersions of 60, 120, and 180 km s<sup>-1</sup> and adjusting  $\lambda$  and  $\sigma$  parameters corresponding to their ages and metallicities (see Eq. 2) by 0.05 dex. For example, for the (5 Gyr, -0.3 dex) "reference SSP" the pairs were constructed using (5.33 Gyr, -0.258 dex) and (5.50 Gyr, -0.328 dex) respectively. Later, these models were fit against their "reference SSPs" using the PPF procedure by Cappellari & Emsellem (2004) with the 13th order multiplicative polynomial continuum. The fitting residuals obtained by this procedure correspond to the quantity defined in Eq. 3.

We have co-added the information on  $\lambda$  and  $\sigma$  sensitivity in 20 Å bins in the wavelength range between 4700 and 5600 Å and normalised it by the total value of non-reduced  $\chi^2$  thus obtaining the relative importance of every 20 Å-wide bin to the determination of the stellar population parameters. Four examples with different stellar populations and velocity dispersions are provided in Fig 2. One should not directly compare blue and red curves, because they represent the normalised quantities: the absolute values of  $S(\lambda; t; Z; \sigma)$  as defined by Eq. 3 are several times higher than  $S(\lambda; t; Z; \sigma)$  explaining the elongated shapes of the 1- $\sigma$  uncertainty ellipses in the age-metallicity space.

As expected, the most valuable information is contained in prominent absorption-line features such as H $\delta$  and Mgb having corresponding Lick indices defined. However, it is noticeable that  $\lambda$  and  $\sigma$ -sensitive information is present everywhere in the spectrum although in different amounts. Going to low metallicities or young ages, thus, reducing the absorption-line features apart from H $\delta$ , causes concentration of information in the most prominent lines. Increasing the intrinsic velocity dispersion also does so by smearing out faint spectral features, therefore for high-resolution spectra of low velocity dispersion objects it is possible to take the full

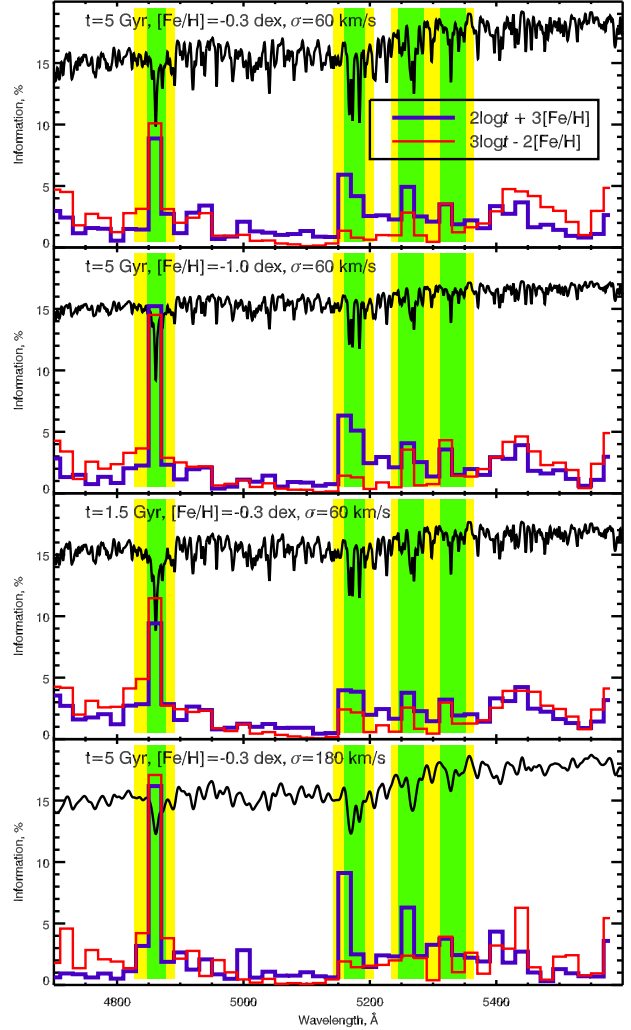


Figure 2. Spectral distribution of the stellar population sensitive information for four stellar populations in 20 Å-wide bins. Corresponding age, metallicity, and velocity dispersion are indicated in every panel. The studied SSPs are shown in black; blue and red histograms display the relative importance of spectral bins (in per cent) for the determination of  $\lambda$  and  $\sigma$  stellar population properties respectively. Green bars denote the bands defining the following Lick indices: H $\delta$ , Mgb, Fe5270, and Fe5335 with yellow side-bars corresponding to the corresponding pseudo-continuum definition regions.

advantage of techniques such as NBURSTs over line-strength indices.

To be stressed that in none of the presented examples the 20 Å-wide bin around H $\delta$  contains even 20 per cent of the  $\lambda$ -sensitive information. This explains why it is possible to precisely constrain the stellar population age using full spectral fitting techniques even if H $\delta$  (or other Balmer lines) are not available (Chilingarian et al. 2008a,c).

To measure the metallicity gradients we fit the co-added spectra in the two regions along the radius adding the data on both sides of the galaxy centre, individually selected for every object. With our data it is not possible to define the regions automatically based only on the values of  $r_e$ , because the effective surface brightness values as well as exposure times differ quite significantly from object to object, leading

to very different signal-to-noise ratios at a given distance from the centre in terms of  $r_e$ . Therefore, we based the definitions of the radial zones based on the observed radius of a nucleus  $r_{nuc}$  defined as a half-size of a pronounced bump in the metallicity profile, if observed or 1.5 arcsec otherwise, resulting in a range of values from 1.5 to 4 arcsec (for VCC 478). The inner radius of the inner region was chosen to be  $r_{ii} = 1.5r_{nuc}$  to prevent the contamination of the spectra by the light of a galactic nucleus, but not smaller than 3.5 arcsec. The outer radius of the inner region and the parameters of the outer region were defined as follows:  $r_{io} = (2.5=1.5)r_{ii}$ ;  $r_{oi} = (3.5=1.5)r_{ii}$ ;  $r_{oo} = (5.5=1.5)r_{ii}$ . At the end, inner and outer regions turned to be about 1/4 to 1/2 and 1/2 to 1 in the units of effective radii. The values of the metallicity gradients were computed as  $[Fe/H]_r = 2([Fe/H]_o - [Fe/H]_i)/(r_{oi} + r_{oo} - (r_{ii} + r_{io}))$ , where  $[Fe/H]_i$  and  $[Fe/H]_o$  are the values of metallicity derived from the fitting of the co-added spectra in the inner and outer regions along the radius. Then, the values were converted into  $[Fe/H]$  per  $r_e$  and per kpc.

We computed the radial variations of the B-band stellar mass-to-light ratios using the `pegase.2` (Floc & Rocca-Volmange 1997) code for the Salpeter IMF. It is important to mention that according to the predictions of `pegase.2`, in addition to the stellar content, another 30 to 40 per cent of the mass is supposed to be contained in the form of ISM. The cluster dwarf elliptical galaxies are supposed to efficiently lose their ISM in quite short time by means of gravitational harassment (see e.g. Moore et al. 1996) or ram-pressure stripping (see e.g. Abadi et al. 1999). Therefore, to estimate the mass-to-light ratios of the stellar populations we do not take into account this gas mass. The two other remaining components of the total SSP mass, white dwarfs and neutron stars / black holes are taken into account.

The parameters referred throughout the paper as "periphery" or "main galactic body" were obtained from the co-added spectra along the slit on both sides of the photometric nuclei of galaxies at radii from  $r_{ii}$  to  $r_{oo}$ .

For the objects having spectra with sufficient signal-to-noise ratios in the blue spectral range we also measured the Lick indices. We compared the measurements of  $Mgb$  and the combined iron index  $HFei = 0.72Fe_{5270} + 0.28Fe_{5335}$  (Thomas et al. 2003) with the SSP models for different enhancement presented in the same study. These measurements were made in the nuclear and peripheral parts of the galaxies, as well as for all the SDSS DR6 spectra. To measure the Lick indices we have transformed the data into the Lick system by convolving the spectra with the quadratic difference of the Lick spectral resolution and the effective spectral resolution of the data (instrumental resolution and the intrinsic broadening due to velocity dispersion of the galaxies), as was proposed by Kuntschner (2004) and applied to the SDSS data, e.g. in Chilingarian et al. (2008c).<sup>2</sup> We derived the values of the  $[Fe/H]$  abundance ratios by inverting the

grids of models presented in Thomas et al. (2003) using the age values obtained from the full spectral fitting procedure described above.

## 4 RESULTS

In Table 2 we present the kinematical and stellar population properties of the galaxies in our sample. We provide the global photometric parameters, absolute magnitudes  $M_B$  corrected for the Galactic extinction and half-light radii  $r_e$  from the literature. The conversion from the photometric systems in the original bibliographic sources to the B band was done using the transformations of Fukugita et al. (1995). We compiled the photometric measurements from the following studies (see Table 1): the ACS Virgo Cluster Survey (Ferrarese et al. 2006), the Keck dE project (Geha et al. 2002, 2003), HST WFPC2 surface photometry (Stiavelli et al. 2001), Palomar dE project (van Zee et al. 2004b,a), SDSS DR6 (Adelman-McCarthy et al. 2008). From the SDSS DR6 catalogue we have adopted the values of the  $g^0$ -band 50-percentile Petrosian radius as  $r_e$ . We have used the distance modulus of the Virgo cluster 31.09 mag, as in Ferrarese et al. (2006), and respectively corrected the absolute magnitudes from other studies.

The following quantities are provided for the nuclear regions and main bodies of the galaxies: velocity dispersion, luminosity-weighted age, metallicity, stellar mass-to-light ratios assuming the Salpeter IMF,  $[Mg/Fe]$  abundance ratio. We also provide metallicity gradients per kpc and  $r_e$ , computed as described above.

Since the stellar population properties estimated by the full spectral fitting are a subject to the age(metallicity degeneracy), we provide the uncertainties in the rotated coordinate system (see Eq. 2). The two pairs of columns, and

provide a possibility to recover the approximate dimensions of the inclined error ellipses in the age(metallicity) plot for the nuclear and peripheral parts of the galaxies.

### 4.1 Comparison of the Datasets

For the long-slit and IFU datasets we have fit the co-added spectra of the central regions of the galaxies in the 3 arcsec-wide aperture in order to compare the derived stellar population properties directly with those obtained from the fitting of the SDSS spectra. In Fig 3 we compare these measurements. The agreement is very good showing no systematic offsets between the different datasets, which suggests that the data were reduced properly. Since there is no systematic offset in the metallicity estimates, we conclude that the subtraction of additive background components, such as diffuse light in the spectrograph or the sky background, was precise. This is an important conclusion, that SDSS spectra allow us to study the stellar population properties of dE/dS0 nuclei. Although the spectra are contaminated by the light of main galactic discs/spheroids, the results obtained from the full spectral fitting of SDSS spectra are fairly consistent with those obtained from the analysis of other ground-based data, giving possibility to study much broader samples of dwarf early-type galaxies using only SDSS data.

For the three objects, VCC 543, VCC 1036, and VCC 1122 having long-slit data in both, Palomar dE project

<sup>2</sup> Since we did not have sufficient number of observations of Lick standard stars, no systematic offsets between our data and the original Lick/IDS response function (see e.g. Appendix A of Michielsen et al. 2008) could be calculated and applied to our measurements of the Lick indices.



Table 2. Kinematical and stellar population properties of dwarf early-type galaxies: circumnuclear regions. The columns are as follows: object name, absolute magnitude (extinction corrected), effective radius, adopted nuclear radius, central velocity dispersion, age, metallicity, 2 columns representing uncertainties of stellar population parameters (see text), central [M g/Fe] abundance ratio, B-band mass-to-light ratio, 2 columns providing ages and metallicities from the fitting of SDSS DR6 spectra.

VCC	$M_B$ mag	$r_e$ arcsec	$r_n$ arcsec	$\sigma_0$ km s <sup>-1</sup>	$t$ Gyr	[Fe/H] dex			[M g/Fe] dex	( $M=L$ ) <sub>B</sub> ( $M=L$ )	$t_{SDSS}$ Gyr	[Fe/H] <sub>SDSS</sub> dex
0178	-15.43	8.7	2.0	50 2	10.6	-0.73	0.08	0.03	0.14 0.05	4.8	8.5 2.0	-0.81 0.04
0389 <sup>a</sup>	-16.28	10.9	2.5	23 3	3.9	-0.38	0.09	0.07	::: :::	2.8	3.6 0.4	-0.27 0.03
0389 <sup>a</sup>	-16.28	10.9	2.5	36 2	4.9	-0.30	0.10	0.04	::: :::	3.6	3.6 0.4	-0.27 0.03
0437	-16.85	25.1	4.0	47 1	4.5	-0.36	0.04	0.02	0.06 0.05	3.2	:::	:::
0490 <sup>a</sup>	-16.14	17.4	17.4	33 5	5.1	-0.23	0.23	0.09	::: :::	3.9	2.4 0.3	-0.15 0.03
0490 <sup>b</sup>	-16.14	17.4	1.5	34 8	3.3	-0.35	0.13	0.04	::: :::	2.4	2.4 0.3	-0.15 0.03
0543	-16.55	17.1	2.0	49 1	5.4	-0.49	0.06	0.01	0.09 0.06	3.2	4.9 0.7	-0.30 0.03
0543 <sup>a</sup>	-16.55	17.9	2.0	48 3	5.7	-0.41	0.14	0.04	::: :::	3.6	4.9 0.7	-0.30 0.03
0545 <sup>a</sup>	-15.10	9.5	9.5	31 7	5.1	-0.47	0.27	0.07	::: :::	3.2	9.3 2.9	-0.79 0.05
0634 <sup>a</sup>	-16.31	16.6	2.5	26 2	4.0	-0.30	0.13	0.07	::: :::	3.1	2.5 0.3	-0.17 0.03
0856 <sup>a</sup>	-16.42	14.7	2.5	31 1	5.0	-0.43	0.10	0.03	0.06 0.12	3.2	4.1 0.6	-0.39 0.03
0917	-15.48	7.8	2.0	41 1	4.4	-0.62	0.05	0.02	0.03 0.04	2.6	4.9 0.8	-0.48 0.02
0965	-15.44	13.8	1.5	34 4	2.2	-0.56	0.12	0.04	-0.14 0.07	1.4	3.0 1.2	-0.66 0.10
0990	-16.31	9.7	2.0	53 1	4.0	-0.40	0.03	0.02	0.06 0.03	2.8	4.1 0.5	-0.32 0.03
1010 <sup>a</sup>	-16.79	22.9	2.5	43 2	7.3	-0.33	0.10	0.04	0.03 0.09	4.8	:::	:::
1036	-17.03	14.6	1.5	53 1	3.5	-0.15	0.02	0.01	-0.05 0.03	3.0	3.0 0.2	-0.02 0.02
1036 <sup>a</sup>	-17.03	14.6	1.5	41 2	2.6	-0.02	0.09	0.04	::: :::	2.4	3.0 0.2	-0.02 0.02
1075	-15.71	14.6	1.5	53 7	5.7	-0.74	0.22	0.06	::: :::	2.8	7.9 3.6	-0.77 0.07
1087 <sup>a</sup>	-16.80	18.9	2.5	63 4	5.3	-0.27	0.13	0.04	::: :::	3.9	5.2 0.8	-0.22 0.02
1122	-16.03	11.4	2.5	40 1	2.4	-0.37	0.04	0.01	0.05 0.05	1.7	2.6 0.4	-0.28 0.02
1122 <sup>a</sup>	-16.03	11.4	2.5	33 1	2.4	-0.30	0.09	0.03	::: :::	1.9	2.6 0.4	-0.28 0.02
1183 <sup>a</sup>	-16.66	10.5	2.5	56 2	4.7	-0.28	0.08	0.03	::: :::	3.6	:::	:::
1250 <sup>a</sup>	-18.27	16.2	2.5	79 4	2.2	-0.07	0.11	0.04	-0.02 0.15	2.0	2.8 0.1	-0.05 0.01
1261	-17.38	21.1	2.5	54 1	2.5	-0.27	0.02	0.01	-0.06 0.03	2.0	2.6 0.3	-0.25 0.02
1308	-15.41	9.1	2.0	47 1	3.6	-0.46	0.04	0.03	-0.00 0.07	2.4	:::	:::
1407 <sup>a</sup>	-15.64	8.9	8.9	36 5	5.0	-0.51	0.31	0.07	::: :::	3.1	5.8 1.5	-0.54 0.03
1422 <sup>b</sup>	-17.07	19.3	1.5	44 7	7.1	-0.48	0.09	0.04	::: :::	4.1	5.5 0.8	-0.30 0.02
1491 <sup>a</sup>	-15.44	10.2	2.5	47 4	5.6	-0.44	0.18	0.05	::: :::	3.5	5.4 1.2	-0.33 0.03
1514	-15.58	13.7	2.0	42 3	4.5	-0.77	0.09	0.04	-0.04 0.05	2.3	:::	:::
1545 <sup>b</sup>	-15.90	11.2	1.5	59 5	4.3	-0.05	0.07	0.03	::: :::	3.9	5.5 0.6	-0.16 0.02
1743	-15.20	10.4	10.4	44 8	14.0	-1.01	0.13	0.12	::: :::	5.0	2.9 1.0	-0.46 0.08
1857	-15.85	20.8	20.8	46 16	2.7	-0.66	0.42	0.15	::: :::	1.5	:::	:::
1871 <sup>b</sup>	-16.54	6.9	1.5	68 3	4.9	+0.03	0.04	0.02	-0.02 0.03	4.7	5.7 0.4	+0.11 0.01
2019	-16.25	15.4	1.5	44 1	2.3	-0.28	0.05	0.01	-0.03 0.07	1.8	:::	:::
2048 <sup>a</sup>	-16.85	12.6	2.5	33 2	3.9	-0.44	0.06	0.05	-0.01 0.15	2.7	:::	:::
2050	-15.55	10.8	2.5	32 2	2.6	-0.54	0.06	0.02	-0.17 0.09	1.7	2.5 0.6	-0.28 0.04

<sup>a</sup> Data from the HyperLEDA FITS archive (OHP CARELEC).

<sup>b</sup> IFU spectroscopic data (MPFS).

and the HyperLEDA FITS Archive, the agreement between the derived kinematical and stellar population profiles is fairly good (see details in the following subsection on individual galaxies).

We quantitatively compare our kinematical profiles with the results published in Simien & Prugniel (2002) which are available in the electronic form. In all the cases both, the measurements and the derived uncertainties are absolutely consistent between the two studies although they were obtained using completely different data analysis techniques. We notice that in order to derive the stellar population properties we need higher signal-to-noise ratio than required only to constraint kinematics, therefore we had to apply coarser binning to the data degrading the spatial resolution to a higher degree than that presented in Simien & Prugniel (2002).

Since no kinematical profiles are provided in the

computer-readable form in the other publications presenting dE/dS0 kinematics, we were able to make only qualitative comparison with the published kinematical profiles for some objects.

van Zee et al. (2004b) present two kinematical profiles for every galaxy observed in the course of the Palomar dE project, corresponding to the spectra obtained in the blue and red arms of the Double Spectrograph. The red arm data, having higher spectral resolution and sharper and deeper absorption lines of the Ca II triplet result in higher quality kinematical data, which is clearly seen in Fig 3 of van Zee et al. (2004b). It is also clear from the same figure that the velocity dispersion values obtained from the blue arm spectra are generally systematically above those derived from the red arm data, which is probably caused by the imperfections of the data analysis in low- $\sigma$  regime, where measured velocity dispersions are similar to or lower

Table 3. Kinematical and stellar population properties of dwarf early-type galaxies: external regions. The columns are as follows: object name, velocity dispersion in the periphery, age, metallicity, 2 columns representing uncertainties of stellar population parameters (see text),  $[Mg/Fe]$  abundance ratio, B-band mass-to-light ratio, metallicity gradients per  $r_e$  and per kpc where positive values denote the decrease of  $[Fe/H]$  outwards.

VCC	$\sigma_p$		t	$[Fe/H]$			$[Mg/Fe]$		$(M/L)_B$	$[Fe/H]_r$		$[Fe/H]_r$	
	km	s <sup>-1</sup>	Gyr	dex	dex	dex	dex	dex	( $M/L$ )	dex $r_e^{-1}$	dex $r_e^{-1}$	dex kpc <sup>-1</sup>	dex kpc <sup>-1</sup>
0178	39	3	11.5	-0.83	0.09	0.05	0.07	0.05	4.8	0.48	0.20	0.68	0.29
0389 <sup>a</sup>	17	6	3.7	-0.35	0.15	0.13	:::	:::	2.7	:::	:::	:::	:::
0389 <sup>a</sup>	23	4	3.2	-0.44	0.17	0.15	:::	:::	2.1	:::	:::	:::	:::
0437	44	3	17.9	-1.04	0.03	0.05	0.20	0.07	5.8	0.91	0.11	0.45	0.05
0490 <sup>a</sup>	:::	:::	:::	:::	:::	:::	:::	:::	:::	:::	:::	:::	:::
0490 <sup>b</sup>	29	7	12.8	-0.79	0.23	0.12	:::	:::	5.4	:::	:::	:::	:::
0543	44	2	7.3	-0.69	0.07	0.03	0.16	0.06	3.6	0.37	0.17	0.27	0.13
0543 <sup>a</sup>	48	4	6.4	-0.63	0.17	0.06	:::	:::	3.3	:::	:::	:::	:::
0545 <sup>a</sup>	:::	:::	:::	:::	:::	:::	:::	:::	:::	:::	:::	:::	:::
0634 <sup>a</sup>	31	4	2.1	-0.11	0.12	0.04	:::	:::	1.9	:::	:::	:::	:::
0856 <sup>a</sup>	31	2	5.9	-0.45	0.14	0.04	:::	:::	3.6	:::	:::	:::	:::
0917	42	3	10.9	-1.00	0.10	0.05	-0.01	0.06	4.2	0.21	0.19	0.33	0.31
0965	12	15	6.5	-1.01	0.17	0.07	:::	:::	2.7	0.55	0.29	0.50	0.26
0990	51	1	5.1	-0.59	0.06	0.01	0.16	0.04	2.9	0.20	0.06	0.25	0.08
1010 <sup>a</sup>	49	2	7.7	-0.40	0.12	0.04	-0.06	0.11	4.8	:::	:::	:::	:::
1036	56	1	4.9	-0.33	0.03	0.01	0.17	0.03	3.5	0.48	0.06	0.41	0.05
1036 <sup>a</sup>	43	3	2.9	-0.13	0.11	0.04	:::	:::	2.4	:::	:::	:::	:::
1075	41	7	5.0	-0.52	0.22	0.05	:::	:::	3.1	-0.09	0.23	-0.08	0.19
1087 <sup>a</sup>	65	5	13.8	-0.60	0.21	0.15	:::	:::	6.5	:::	:::	:::	:::
1122	39	2	6.7	-0.82	0.07	0.03	0.09	0.06	3.1	0.38	0.10	0.42	0.11
1122 <sup>a</sup>	35	3	3.8	-0.55	0.08	0.08	:::	:::	2.3	:::	:::	:::	:::
1183 <sup>a</sup>	65	5	8.3	-0.52	0.17	0.06	:::	:::	4.6	:::	:::	:::	:::
1250 <sup>a</sup>	80	3	2.3	-0.05	0.08	0.03	0.11	0.11	2.1	:::	:::	:::	:::
1261	57	1	4.9	-0.61	0.05	0.01	0.24	0.04	2.8	0.40	0.10	0.24	0.06
1308	45	3	5.9	-0.75	0.09	0.02	0.02	0.06	2.9	0.38	0.10	0.52	0.13
1407 <sup>a</sup>	:::	:::	:::	:::	:::	:::	:::	:::	:::	:::	:::	:::	:::
1422 <sup>b</sup>	50	3	4.8	-0.40	0.03	0.01	:::	:::	3.3	:::	:::	:::	:::
1491 <sup>a</sup>	37	8	7.4	-0.57	0.31	0.14	:::	:::	4.0	:::	:::	:::	:::
1514	48	3	3.0	-0.64	0.09	0.07	0.11	0.06	1.7	:::	:::	:::	:::
1545 <sup>b</sup>	64	4	8.3	-0.40	0.06	0.03	:::	:::	5.1	:::	:::	:::	:::
1743	:::	:::	:::	:::	:::	:::	:::	:::	:::	:::	:::	:::	:::
1857	:::	:::	:::	:::	:::	:::	:::	:::	:::	:::	:::	:::	:::
1871 <sup>b</sup>	65	4	5.0	-0.14	0.06	0.03	0.01	0.06	4.2	:::	:::	:::	:::
2019	42	3	3.5	-0.54	0.05	0.05	-0.04	0.10	2.2	-0.19	0.16	-0.15	0.13
2048 <sup>a</sup>	39	3	2.9	-0.45	0.10	0.04	-0.09	0.13	1.9	:::	:::	:::	:::
2050	21	5	4.5	-0.76	0.11	0.04	0.03	0.09	2.3	0.20	0.16	0.23	0.19

<sup>a</sup> Data from the HyperLEDA FITS archive (OHP CARELEC).

<sup>b</sup> IFU spectroscopic data (MPFS).

than the instrumental resolution. Our analysis of the blue arm spectra in terms of kinematics turns to be much more precise than what is presented in van Zee et al. (2004b). In the central regions of the galaxies our velocity dispersion profiles agree remarkably well with those derived from the higher resolution red arm spectra by van Zee et al. (2004b), whereas in the peripheral parts we usually reach even higher quality of measurements evident from the lower scatter of the values. The two exceptions are VCC 956 and VCC 2050, where velocity dispersions are too low to be extracted from blue arm spectra.

The kinematical profiles of several galaxies included in our sample were presented in the literature. The rotation profiles agree well for VCC 543 and VCC 1010 displayed in Fig 2 of Pedraz et al. (2002), while in VCC 1122 we see somewhat higher degree of rotation. The velocity dispersion values are consistent for all three objects. Their data were

obtained with the IDS spectrograph at the 2.5 Isaac Newton Telescope and had 2.5Å FWHM spectral resolution in the blue spectral range, which is very similar to the datasets we discuss in this paper.

Seven galaxies included in our sample, VCC 543, 856, 917, 1036, 1087, 1261, and 1308 were observed with the Keck ESI spectrograph, and the kinematical analysis was presented in Geha et al. (2002, 2003). The data had considerably higher spectral resolution than ours ( $R \sim 10000$ ) but were localised in the central regions of the galaxies (out to 10 arcsec from the centres) due to a relatively short slit. Both, radial velocity and velocity dispersion profiles for the seven galaxies generally agree, however we notice that the specific details (e.g. -drops) look smeared in the ESI data compared to the Palomar DSS spectra, although one would expect the opposite, given better atmosphere conditions at Mauna Kea. Presently, we do not have an explanation to

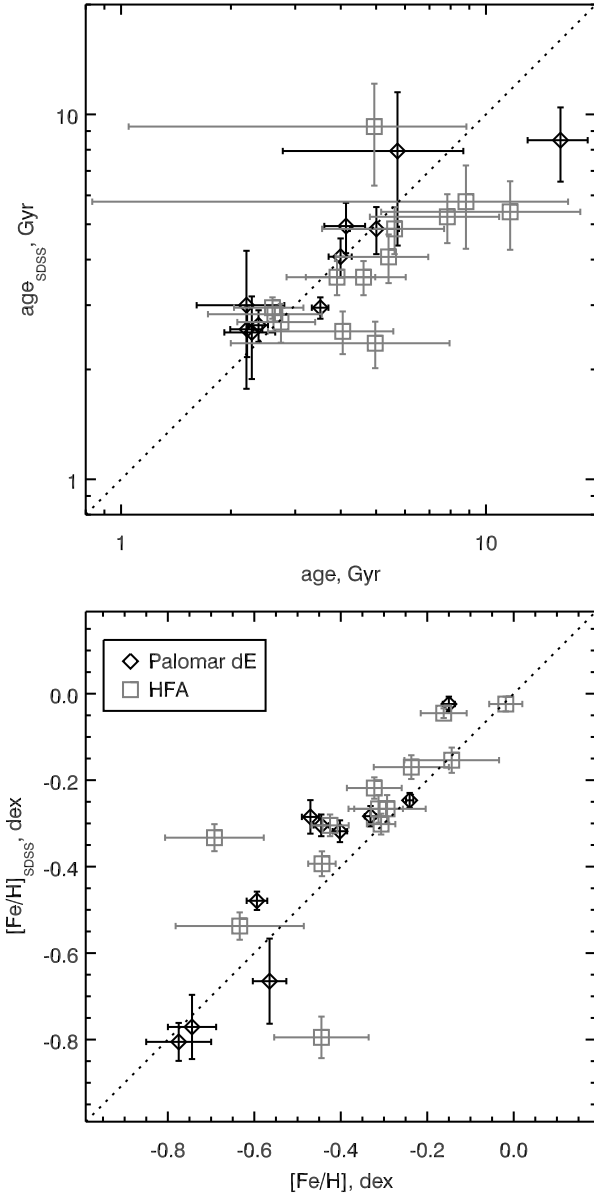


Figure 3. Comparison of age (top panel) and metallicity (bottom panel) measurements in the central parts of the galaxies made on the SDSS DR6 spectra and on the long-slit data. Different symbols correspond to the data from the Palomar dE project and HyperLeda FITS Archive.

this effect, but our guess is that it may be connected to the atmosphere dispersion which would be an order of a few arcsec on a very wide wavelength range of ESI even at moderate air-masses and might smooth the kinematical details if one fits the spectra in the entire wavelength range of the instrument. There is no mentioning about the atmosphere dispersion corrector in the ESI manual available online, neither any information about how it was taken into account in Geha et al. (2002, 2003). Comparing the shapes of the velocity dispersion profiles for VCC 917, 1036, and 1261 in Fig 5 in Geha et al. (2002) and Fig 2 and Fig 3 in Geha et al. (2003), to the data presented in our study one would understand why Geha et al. did not mention the

kinematically-decoupled cores in these galaxies: they were smoothed out.

No spatially-resolved information about the stellar population of the galaxies in our sample is available in the literature. Qualitative comparison of the integrated values with those presented in Geha et al. (2003) and van Zee et al. (2004a) based on the analysis of the line-strength indices results in a good agreement. The statistical comparison of the dE/dS0 stellar population properties with another samples will be given in one of the next papers of the series.

#### 4.2 Notes on Individual Galaxies

Here we briefly describe the results obtained for every galaxy. All cases with spatially-resolved information available are illustrated with the profiles or two-dimensional maps of kinematical and stellar population properties, except VCC 1871, where the colour figures are available in Chilingarian et al. (2007c).

VCC 178 = IC 3081 (Fig 4). This attenuated nucleated dwarf galaxy exhibits significant rotation and quite flat velocity dispersion profile inside  $1 r_e$ . No embedded substructures were revealed by Lisker et al. (2006): VCC 178 is listed in Appendix E there. There is a significant metallicity gradient. Age distribution also demonstrates smooth changes along the radius, being younger in the centre (7 Gyr) than in the periphery (11.5 Gyr).

VCC 389 = IC 781 (Fig 5). This nucleated dE galaxy hosting a "probable disc" reported by Lisker et al. (2006) was observed twice with the CARELEC spectrograph at slightly different positional angles. Both datasets have quite low signal-to-noise ratios, however the derived profiles of the stellar population parameters along the radius agree well. We detected neither statistically significant difference of the stellar population properties in the nucleus and in the main galactic body, nor metallicity gradient.

VCC 437 = UGC 7399A (Fig 6). A very steep metallicity gradient is observed beyond 4 arcsec from the centre. Metallicity at  $1 r_e$  is almost 1 dex lower than at 4 arcsec. Interestingly, at 3 arcsec the  $g^0 - z^0$  colour profile of the galaxy presented in Ferrarese et al. (2006) changes its gradient, and the ellipticity changes drastically. This suggests the presence of an embedded structure in the central part, however, not clearly detected on the unsharp-masked SDSS images, which can be explained if it has nearly face-on orientation. This object is one of the cases, where the luminosity-weighted age also changes along the radius: the population becomes older at larger radii, creating a "conspiracy" effect in the broadband optical colours, making colour profiles looking nearly flat.

VCC 490 = IC 783 (Fig 7). This nucleated dwarf galaxy exhibits prominent spiral arms in the stellar disc (Barazza et al. 2002; Lisker et al. 2006). The HFA data available for this object have very low signal-to-noise ratio outside the nuclear region, therefore the stellar population properties cannot be derived in the periphery of the galaxy. Deep IFU observations were carried out with the MPFS spectrograph in 2004 and presented in Chilingarian (2006) and Chilingarian et al. (2007c). The luminosity-weighted age in the nuclear region of VCC 490 is as young as 3 Gyr, whereas the main galactic body is older than 10 Gyr. There is a hint of a large-scale solid body rotation of the spiral disc

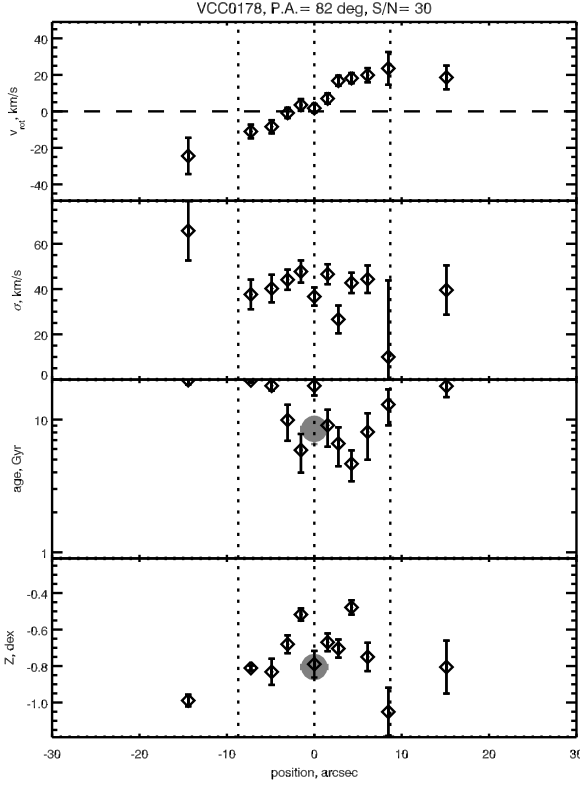


Figure 4. Kinematics and stellar populations of VCC 178 (Palm ar DS). Four panels (from top to bottom) present: radial velocity, velocity dispersion, SSP-equivalent age, and metallicity. Results from the fitting of a SDSS spectrum are shown by filled gray circle. Positional angle of the slit and target signal-to-noise ratio used to adaptively bin the data are indicated. Dotted vertical lines indicate the photometric centre and  $1 r_e$ .

(Simien & Prugniel 2002). The galaxy resides in the periphery of the Virgo cluster, close in projection to the luminous spiral M 100. Their radial velocities are different by only  $270 \text{ km s}^{-1}$  which may suggest the belonging of VCC 490 to the M 100 group.

VCC 543 = UGC 7436 (Fig 8). This flattened rotationally supported galaxy was a subject to the several kinematical studies referenced above. It is one of the three galaxies with the data available both in the Palm ar dE project and in the HFA. The kinematical and stellar population profiles are consistent between the datasets. The age profile in this object is nearly flat with a mean value of  $5.5 \text{ Gyr}$ , while the metallicity exhibits a slight gradient. No embedded structures were detected in this object by Lisker et al. (2006). VCC 545 = IC 783A. No substructures were detected by Lisker et al. (2006) in this faint nucleated dE galaxy. The signal-to-noise ratio of the HFA data was very low so we were able to determine only integrated properties of the stellar populations and mean velocity dispersion, which agree well with the values derived from fitting the SDSS DR6 spectrum. The galaxy is located close in projection to VCC 490 and M 100 and its radial velocity is quite close to that of VCC 490.

VCC 634 = NGC 4328 (Fig 9). This relatively bright rotationally supported nucleated dwarf galaxy does not exhibit embedded structures (Lisker et al. 2006). We see the

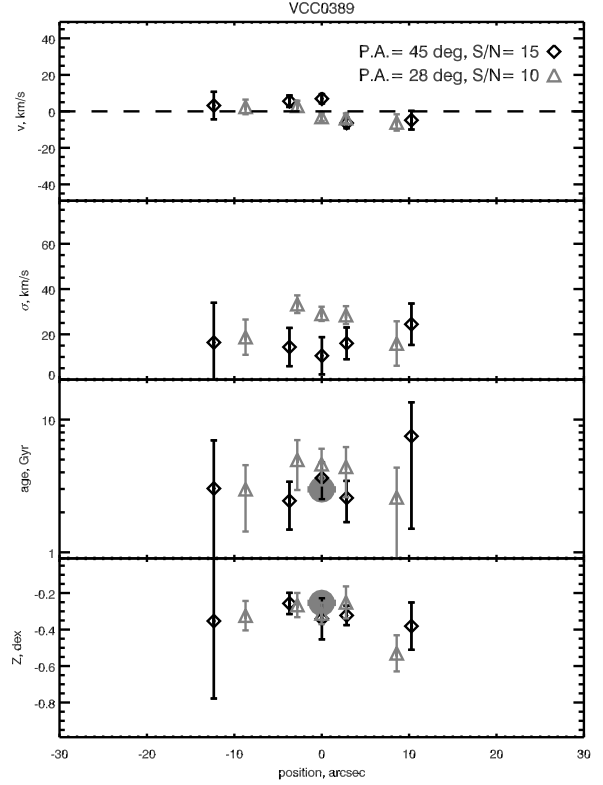


Figure 5. Kinematics and stellar populations of VCC 389 (OHP CARELEC). See Fig 4 for details. Data from two datasets for slightly different positional angles are shown with diamonds and triangles.

intermediate-age ( $3 \text{ Gyr}$ ) quite metal-rich ( $-0.2 \text{ dex}$ ) stellar population without significant changes of the properties within  $1 r_e$ . Low signal-to-noise ratio of the data did not allow us to measure the metallicity behaviour at larger radii. VCC 856 = IC 3328 (Fig 10). This was the first dwarf dE/dS0 galaxy, where low-contrast spiral arms were detected by Jerjen et al. (2000). The data allowed us to derive the stellar population properties out to  $1 r_e$ . The age profile is flat with the mean value of about  $4 \text{ Gyr}$ , whereas the metallicity distribution exhibits a gradient. With the presently available data we were not able to detect any statistically significant difference between the ages of the stellar populations in the nuclear region and in the spiral disc.

VCC 917 = IC 3344 (Fig 11). No substructures were revealed by Lisker et al. (2006) in VCC 917. This flattened object with a very little rotation was considered as one of the examples of the galaxies supported by the anisotropic velocity dispersions. We see a kinematically decoupled central component with the radius of about  $3 \text{ arcsec}$  ( $0.25 \text{ kpc}$ ) rotating in the other sense compared to the main galactic body. It is associated with the drop in the velocity dispersion profile from  $40$  to  $20 \text{ km s}^{-1}$  and younger and much more metal-rich stellar population compared to the periphery. This is the first example of the KDC in a dwarf galaxy supported by anisotropic velocity dispersions.

VCC 965 = IC 3363 (Fig 12). No substructures are reported by Lisker et al. (2006) in this faint flattened nucleated galaxy. This is one of a few cases, where the internal



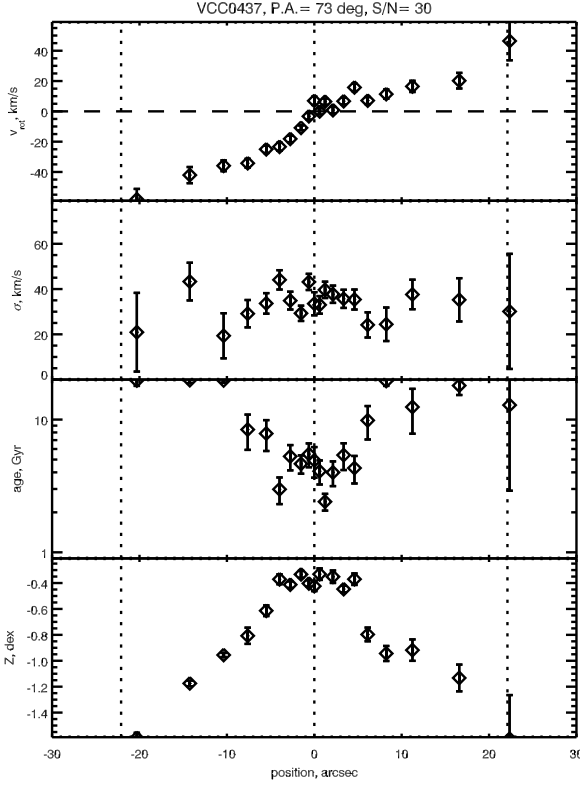


Figure 6. Kinematics and stellar populations of VCC 437 (Palomar DS). See Fig 4 for details.

velocity dispersion is too low to be measured. The stellar population in the nuclear region turns to be very different from the periphery of the galaxy both in terms of young age and high metallicity. The velocity dispersion profile of this object derived from the red arm DS spectra and presented in van Zee et al. (2004b) demonstrates a central velocity dispersion drop.

VCC 990 = IC 3369 (Fig 13). Lisker et al. (2006) report the detection of an inclined disc in this attenuated nucleated galaxy. Inside  $1 r_e$  we see a quite strong metallicity gradient from about 0.3 dex to 0.8 dex while the age remains nearly constant at a level of 5 Gyr. The velocity dispersion distribution exhibits a local minimum in the centre associated with a peculiarity on the radial velocity profile. We detected faint emission lines (H $\beta$ , [O III]) in the fitting residuals suggesting the presence of ionised gas in this galaxy. VCC 1010 = NGC 4431 (Fig 14). Bar and disc were detected in this attenuated rotationally supported galaxy by Lisker et al. (2006). The data available for this object in the HFA allowed us to trace the behaviour of the stellar population parameters out to  $r_e=2$ . Both, age and metallicity distribution look at showing no significant changes along the radius.

VCC 1036 = NGC 4436 (Fig 15). The inclined disc is reported by Lisker et al. (2006). Nearly solid-body rotation out to  $1 r_e$  changes into the flattening of the rotation curve outwards. The velocity dispersion stays constant beyond  $0.3 r_e$  at a level of  $50 \text{ km s}^{-1}$ . This galaxy exhibits a prominent KDC. It is one of the three objects included both in the Palomar dE sample and in the sample of Simien & Prugniel

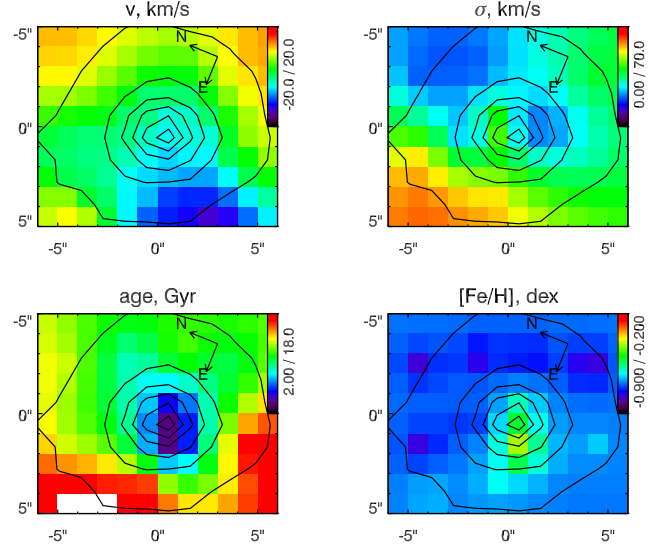


Figure 7. Kinematics and stellar populations of VCC 490 (MPFS). First row: radial velocity and velocity dispersion, second row: age and metallicity. A adaptive binning with the target signal-to-noise ratio of 15 was applied.

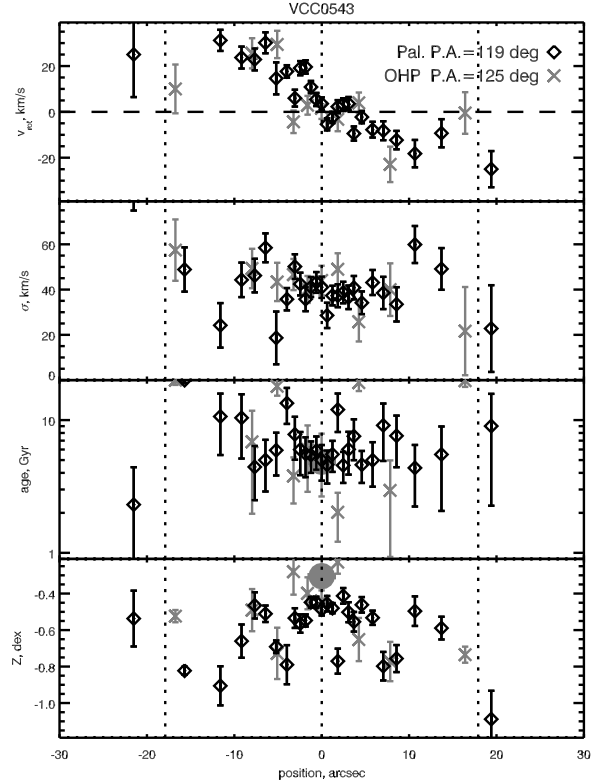


Figure 8. Kinematics and stellar populations of VCC 543 (Palomar DS and OHP CARELEC). Two curves on each panel correspond to the two different datasets. The target signal-to-noise ratios were 20 and 10 for the Palomar DS and OHP datasets respectively. See Fig 4 for details.

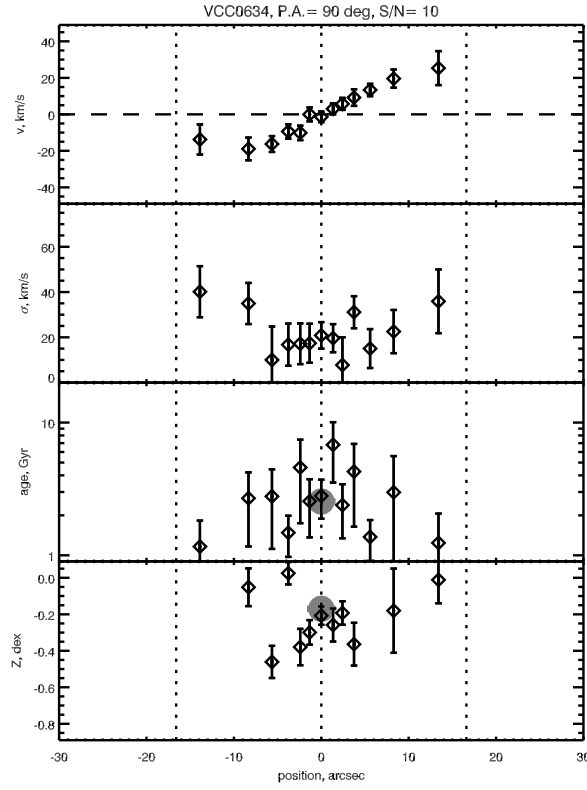


Figure 9. Kinematics and stellar populations of VCC 634 (OHP CARELEC). See Fig 4 for details.

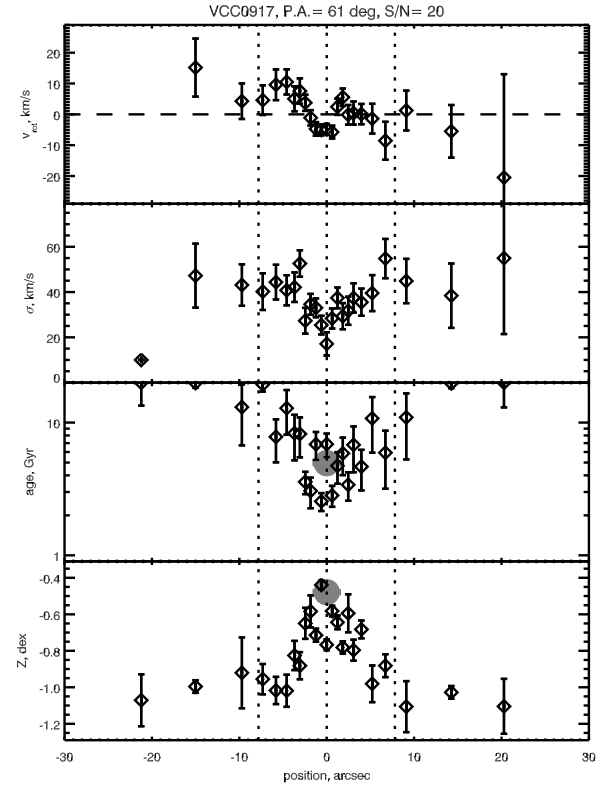


Figure 11. Kinematics and stellar populations of VCC 917 (Palomar DSS). See Fig 4 for details.

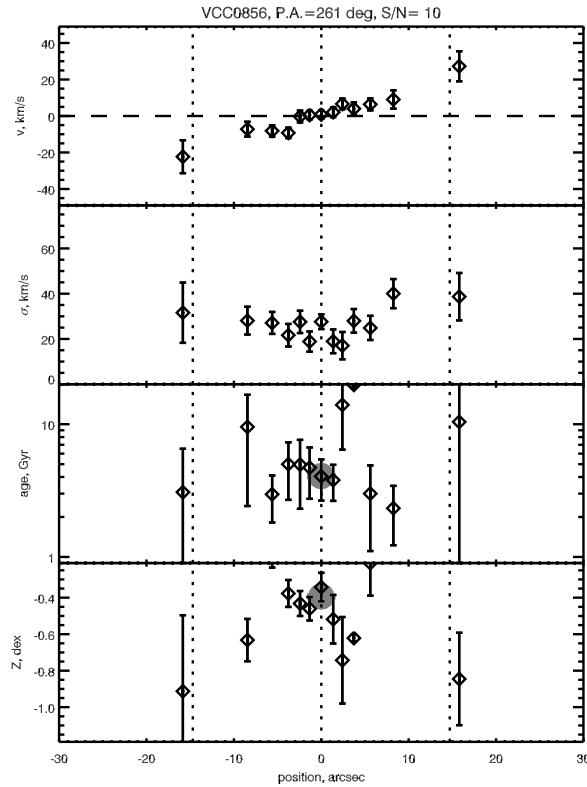


Figure 10. Kinematics and stellar populations of VCC 856 (OHP CARELEC). See Fig 4 for details.

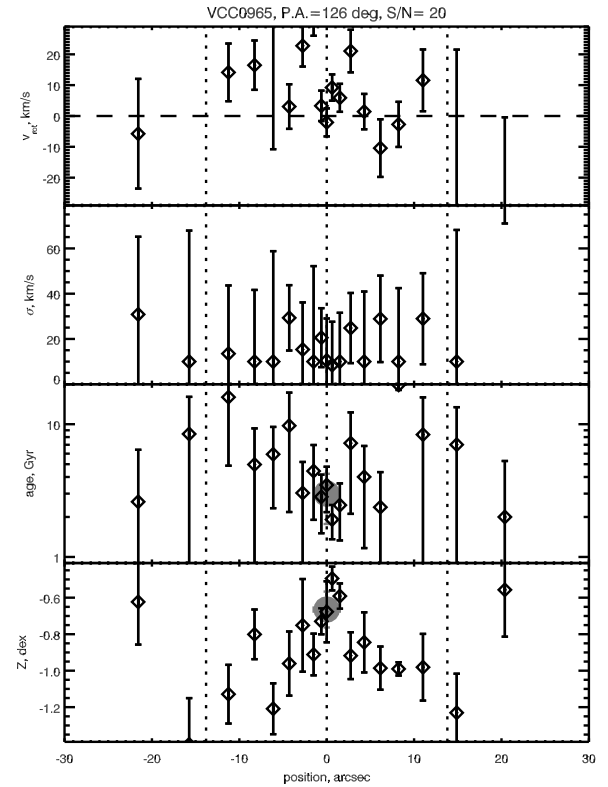


Figure 12. Kinematics and stellar populations of VCC 965 (Palomar DSS). See Fig 4 for details.

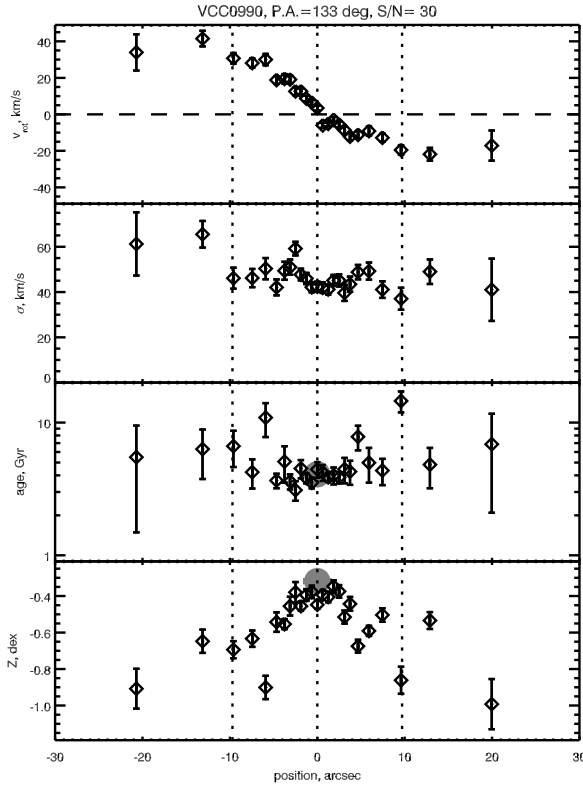


Figure 13. Kinematics and stellar populations of VCC 990 (Palomar DS). See Fig 4 for details.

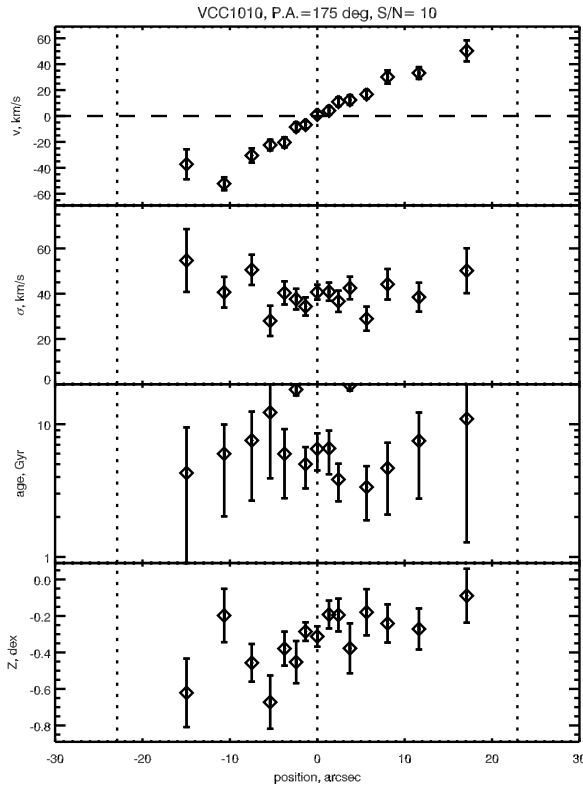


Figure 14. Kinematics and stellar populations of VCC 1010 (OHP CARELEC). See Fig 4 for details.

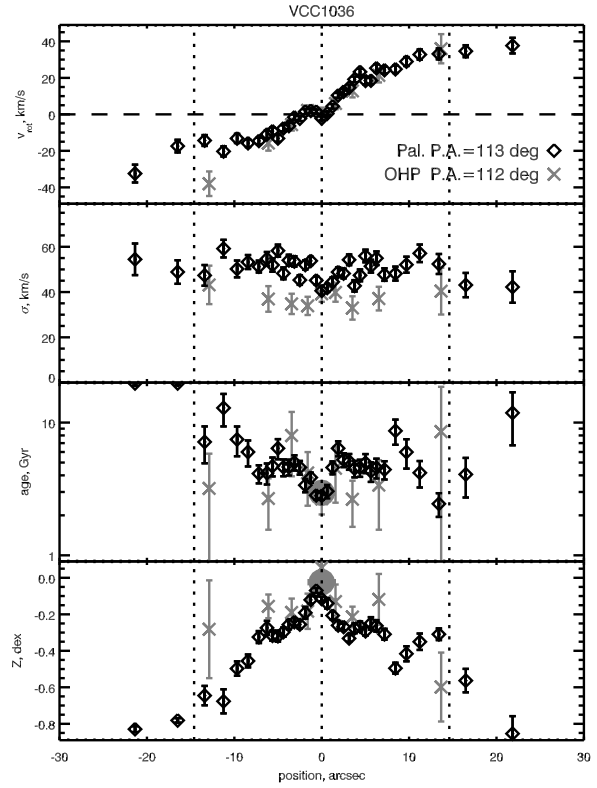


Figure 15. Kinematics and stellar populations of VCC 1036 (Palomar DS and OHP CARELEC). The target signal-to-noise ratios were 30 and 10 for the Palomar DS and OHP datasets respectively. See Fig 8 for details.

(2002). Both datasets agree well on the presence of the kinematically decoupled central component. However, due to worse seeing conditions it is not seen as counter rotation in the HFA data, but as a flat region of the radial velocity profile. A slight depression is seen in the velocity dispersion profile in the region corresponding to the KDC. It corresponds to a pronounced bump in the metallicity profile with the values reaching almost  $[\text{Fe}/\text{H}] = 0.0$  in the SDSS data. SSP-equivalent age ( $\sim 3$  Gyr) in this part is  $\sim 2$  Gyr younger than in the surrounding regions. The metallicity keeps constant at a level about  $-0.3$  dex out to 8 arcsec, then it starts to decrease steeply. This is the only object, where the central value of the  $[\alpha/\text{Fe}]$  abundance ratio ( $-0.05$  dex) differs strongly from the values in the periphery ( $+0.17$  dex). VCC 1075 = IC 3383 (Fig 16). This faint attenuated nucleated dwarf galaxy harbours no embedded substructures according to Lisker et al. (2006). The signal-to-noise ratio of the data is quite low, making difficult to assess the variations of the stellar population parameters along the radius. However, at the present level of precision we do not detect any statistically significant gradients of age neither metallicity. VCC 1087 = IC 3381 (Fig 17). This attenuated nucleated dwarf with no substructures reported by Lisker et al. (2006) has very little if any rotation. The low signal-to-noise ratio of the data makes difficult to study the variations of the stellar population parameters along the radius. We notice that the stellar population parameters derived from the SDSS DR6 spectrum fitting are very different from those estimated from

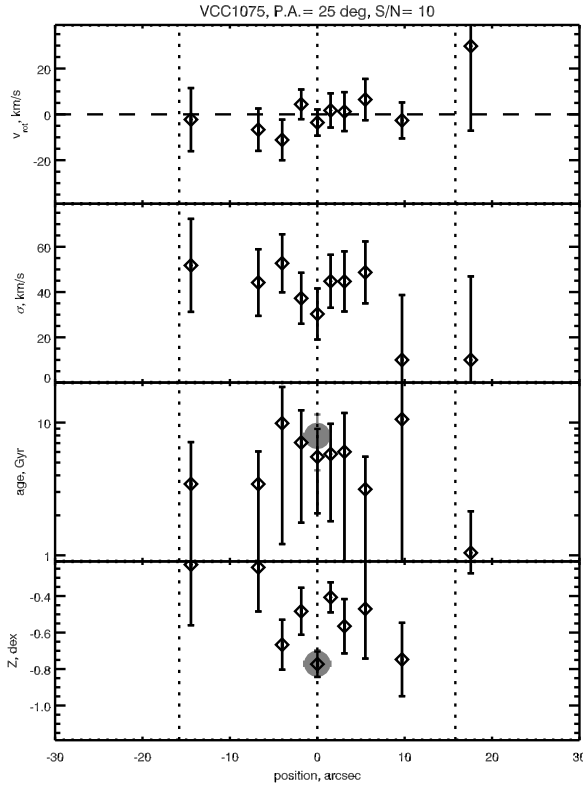


Figure 16. Kinematics and stellar populations of VCC 1075 (Palomar DS). See Fig 4 for details.

the HFA spectra. This, however, may be explained as the seeing effect, which smoothed the nucleus. VCC 1122 = IC 3393 (Fig 18). This strongly attenuated galaxy with the insufficient degree of rotation to be considered as rotationally supported does not exhibit embedded substructures according to Lisker et al. (2006). We have the data from both Palomar DE project and the HFA. The kinematical profiles agree quite well. There is a peculiarity seen in the radial velocity profile 2 arcsec south-east of the nucleus, however presently we do not have enough evidences to interpret it as a kinematically decoupled component. The stellar population properties were determined out to  $2 r_e$  from the Palomar DE data. The nuclear region of VCC 1122 is clearly distinct in both age and metallicity profiles. We also see a remarkable metallicity gradient, which is, however still insufficient to explain the high metallicity in the nuclear region. The age stays constant along the radius beyond  $r_e = 2$ . There are faint H and [O III] emission lines revealed in the fitting residuals localised in the central part of the galaxy. VCC 1183 = IC 3413 (Fig 19). This attenuated nucleated DE galaxy harbours a bar reported by Lisker et al. (2006). We observe some rotation. Low signal-to-noise ratio of the data did not allow the detailed studies of the stellar populations, however we notice the intermediate age ( $\sim 4$  Gyr) and relatively high metallicity ( $\sim 0.3$  dex) without evident changes along the radius.

VCC 1250 = NGC 4476 (Fig 20). This galaxy hosts a large embedded disc with the spiral arms, dust lanes, and H II regions clearly visible on the HST ACS images presented in Ferrarese et al. (2006). Our data covers the re-

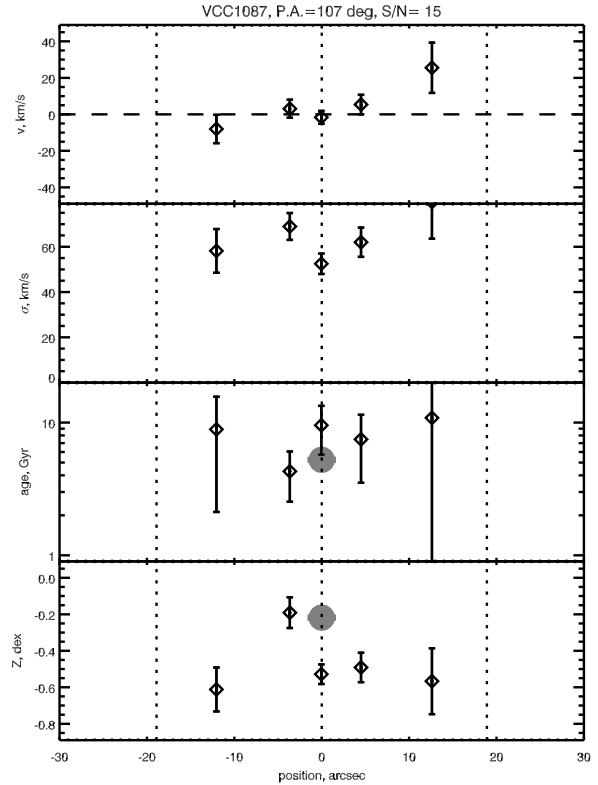


Figure 17. Kinematics and stellar populations of VCC 1087 (OHPCARELEC). See Fig 4 for details.

gion completely dominated by the disc. We see prominent emission lines suggesting on-going star formation. The luminosity weighted age is about 2 Gyr and the metallicity is as high as solar without statistically significant changes along the radius. The B-band absolute magnitude of VCC 1250,  $-18.27$  mag places it at the limit of the infomorph dwarf/giant separation. However, it still can be classified as a low-luminosity early-type galaxy, that's why we included it into our sample.

VCC 1261 = NGC 4482 (Fig 21). No substructures were reported by Lisker et al. (2006) in this galaxy. This object looks like an enlarged version of VCC 917, giving another example of a small rapidly rotating KDC in an attenuated spheroid with a very low, if any, large-scale rotation. As in VCC 917, the KDC is associated with a velocity dispersion drop, younger and much more metal-rich stellar population than in the peripheral parts of the galaxy. Faint emission lines are seen in the fitting residuals, suggesting the presence of warm ISM in this object.

VCC 1308 = IC 3437 (Fig 22). This galaxy was classified as "non-rotating" by Geha et al. (2003) but as "rotating" by van Zee et al. (2004b). No substructures were reported in it by Lisker et al. (2006). We indeed see some rotation, although the radial velocity profile is quite peculiar in the centre, as well as a remarkable metallicity gradient. The stellar population in the central region of the galaxy looks younger than in the outer regions along the radius.

VCC 1407 = IC 3461 Very low signal-to-noise ratio of the data does not allow to study the variations of the stellar population properties along the radius. However, we stress



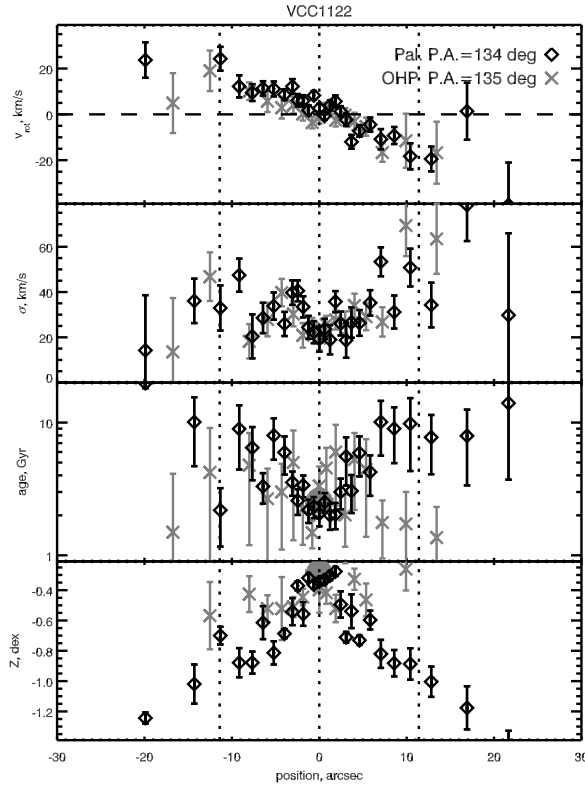


Figure 18. Kinematics and stellar populations of VCC 1122 (Palomar DS and OHP CARELEC). The target signal-to-noise ratios were 30 and 10 for the Palomar DS and OHP datasets respectively. See Fig 8 for details.

a very good agreement of the age and metallicity estimates for this object obtained from the fitting of the HFA and SDSS DR6 spectra. No embedded structures were reported in this galaxy by Lisker et al. (2006).

VCC 1422 = IC 3468 (Fig 23). An embedded structure is detected in this galaxy interpreted as a bar by Barazza et al. (2002) or as an edge-on disc by Lisker et al. (2006). The IFU spectroscopy reveals complex kinematics with evidences for rotation only beyond 5 arcsec from the centre. There is a hint that stellar population in the region of the disc/bar is somewhat younger than in the periphery of the galaxy ( $v = 54 \pm 4 \text{ km s}^{-1}$ ,  $t = 7.2 \text{ Gyr}$ ,  $[\text{Fe}/\text{H}] = -0.54 \text{ dex}$ ), although the difference is on the limit of detection. VCC 1422 is the only galaxy in our sample, where the very central region, dominated by the light of its nucleus exhibits older and more metal-poor stellar population than one of the surrounding disc/bar clearly visible on the maps. Its age and metallicity are found to be very close to those in the periphery of the galaxy.

VCC 1491 = IC 3486 (Fig 24). No substructures were revealed by Lisker et al. (2006) in this non-nucleated galaxy demonstrating quite high degree of rotation for its moderate attening. The stellar population is old ( $8 \text{ Gyr}$ ) and metal-poor ( $-0.6 \text{ dex}$ ) without noticeable gradients.

VCC 1514 = PGC 41726 (Fig 25). Possible inclined disc was reported by Lisker et al. (2006) in this strongly attened galaxy. We observe some rotation. The age and metallicity estimates do not exhibit statistically significant variations

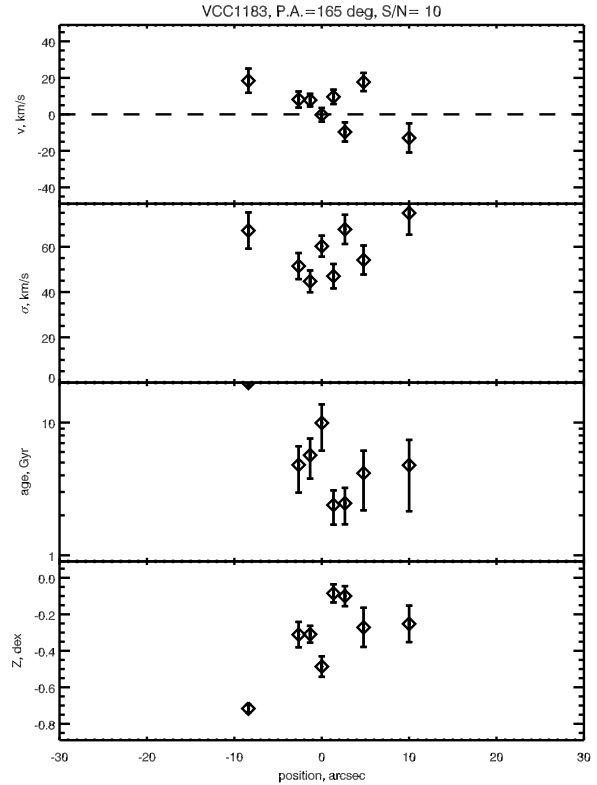


Figure 19. Kinematics and stellar populations of VCC 1183 (OHP CARELEC). See Fig 4 for details.

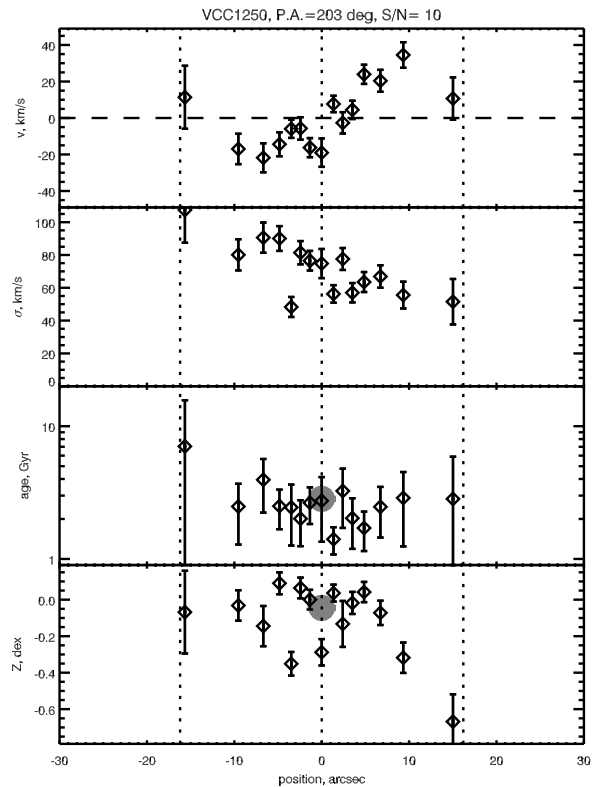


Figure 20. Kinematics and stellar populations of VCC 1250 (OHP CARELEC). See Fig 4 for details.

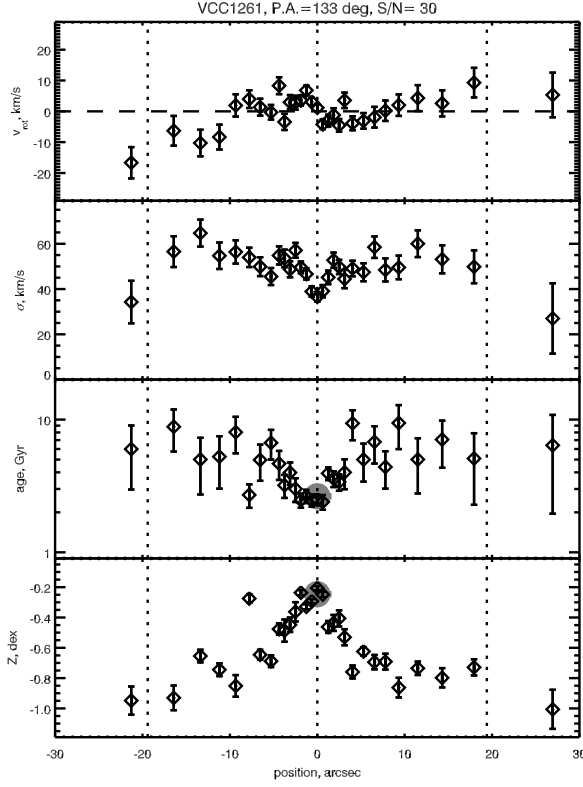


Figure 21. Kinematics and stellar populations of VCC 1261 (Palomar DSS). See Fig 4 for details.

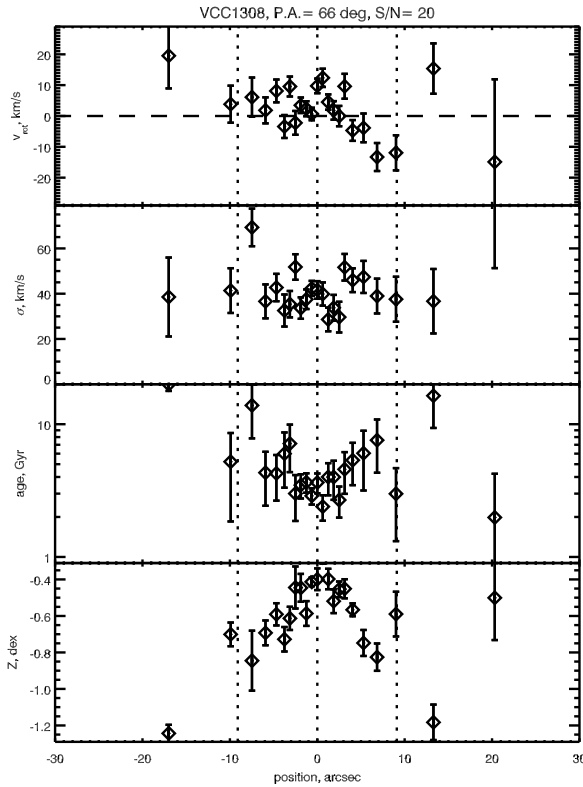


Figure 22. Kinematics and stellar populations of VCC 1308 (Palomar DSS). See Fig 4 for details.

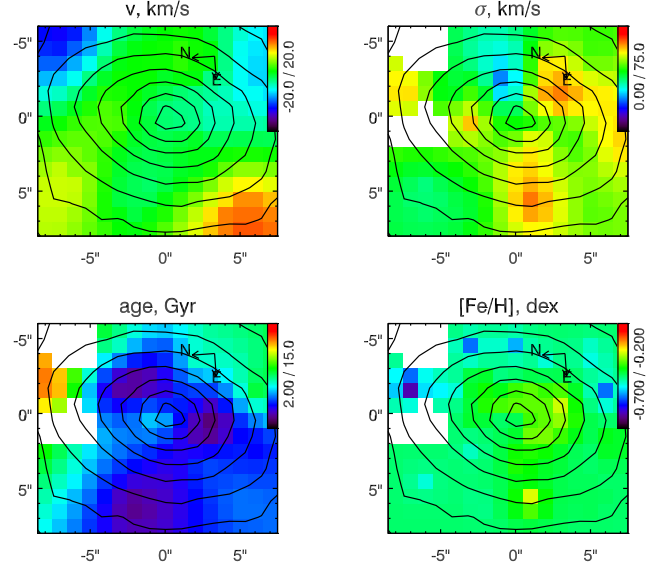


Figure 23. Kinematics and stellar populations of VCC 1422 (MPFS). Panels are the same as in Fig 7. A adaptive binning with the target signal-to-noise ratio of 15 was applied.

along the radius, although the signal-to-noise ratio of the data was rather low.

VCC 1545 = IC 3509 (Fig 26). This galaxy was among the first, where the young stellar population in the central region was reported by Chilingarian et al. (2007d). It demonstrates very complex kinematics: we see a minor-axis rotation (i.e. kinematical decoupling) in the circumnuclear region of the galaxy with the depression in the velocity dispersion distribution there, while there is a large-scale major-axis rotation as well. The stellar population in the nuclear region is younger and considerably more metal-rich than in the main galactic body.

VCC 1743 = IC 3602 This is a faint attenuated dwarf galaxy with the faint extended nucleus seen on the HST ACS images but not on the ground-based data. The galaxy is listed in Appendix E of Lisker et al. (2006) as an object "in which substructure other than a disc was found". The data available to us have very low signal-to-noise ratio due to low surface brightness of the galaxy, therefore we were not able to derive detailed profiles of the stellar population properties. However, outside the nuclear region the age looks to be old ( $\sim 10$  Gyr) and the metallicity quite low ( $-0.6$  dex).

VCC 1857 = IC 3647 The faintest object in the Palomar DE sample does not exhibit and substructures reported by Lisker et al. (2006). The signal-to-noise is not sufficient even for the precise integrated measurements of the stellar populations, however at 1- $\sigma$  confidence level the galaxy has and intermediate age not older than 7 Gyr.

VCC 1871 = IC 3653 An inclined stellar disc was discovered in the velocity field by Chilingarian et al. (2007c) with a counterpart in the colour map. The galaxy has somewhat high surface brightness, the age distribution is nearly uniform, whereas there is a pronounced peak in the metallicity map with the values slightly exceeding solar.

VCC 2019 = IC 3735 (Fig 27). A "possible inclined disc, maybe warped or distorted" is reported in this galaxy by Lisker et al. (2006). The isophotes demonstrate the change

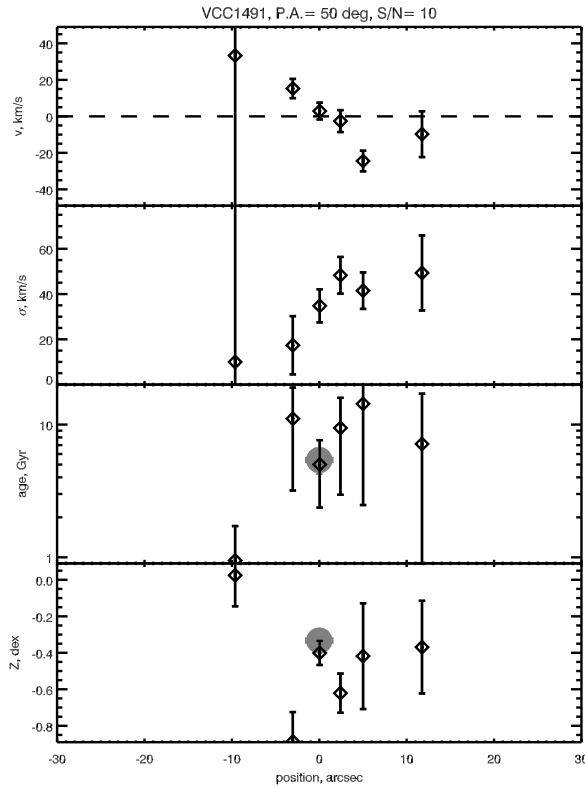


Figure 24. Kinematics and stellar populations of VCC 1491 (OHP CARELEC). See Fig 4 for details.

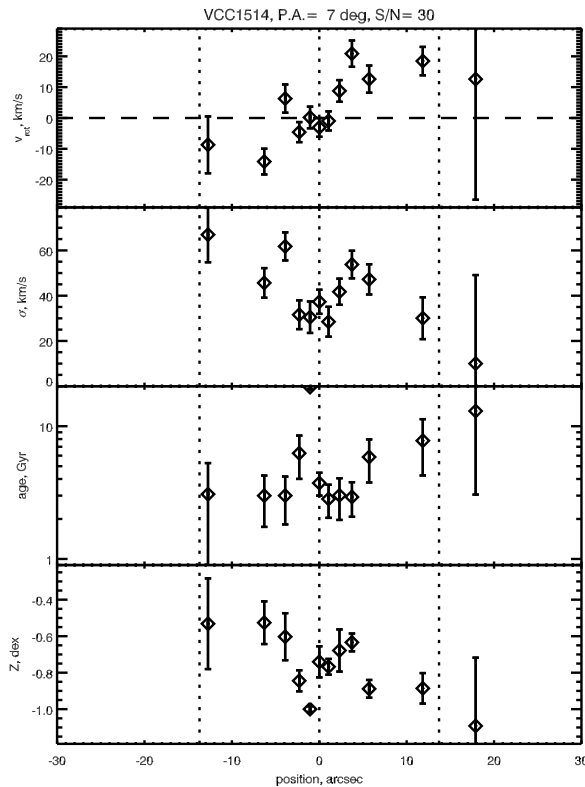


Figure 25. Kinematics and stellar populations of VCC 1514 (Palomar DS). See Fig 4 for details.

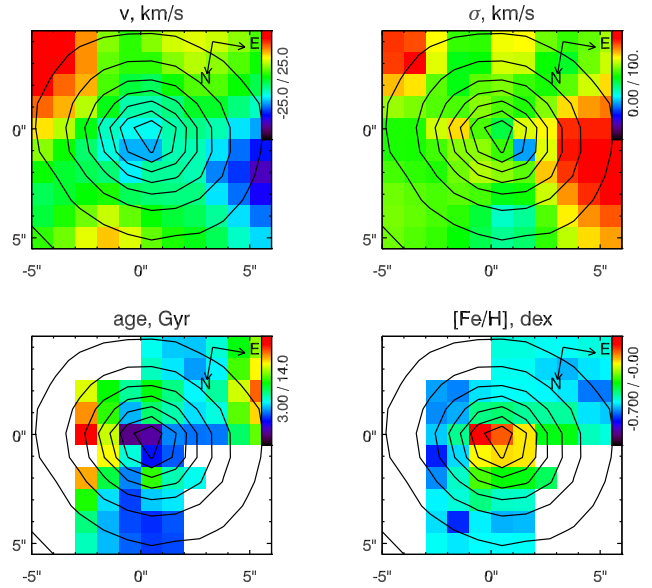


Figure 26. Kinematics and stellar populations of VCC 1545 (MPFS). Panels are the same as in Fig 7. A adaptive binning with the target signal-to-noise ratio of 15 was applied.

of ellipticity and positional angle (Ferrarese et al. 2006). We see a central peak in the metallicity distribution and the corresponding drop in the velocity dispersion profile, while the quality of the age measurements is not sufficient to clearly say whether the nucleus harbours younger stellar population than the outer parts of the galaxy. A noticeable metallicity gradient is observed. We detected faint emission lines (H and [O III]) in the fitting residuals.

VCC 2048 = IC 3773 (Fig 28). There is an evidence for a bar or edge-on embedded disc reported by Lisker et al. (2006). This nucleated galaxy is strongly attenuated. Its inner region, corresponding to the disc demonstrates fast solid-body rotation and looks kinematically decoupled from the outer parts of the galaxy rotating in the same sense, similar to the structures observed by Derijcke et al. (2004) in the two dE galaxies in groups. There is a pronounced drop in the central region of the galaxy. Stellar population properties do not show statistically significant changes along the radius apart from the little region 4 arcsec North of the nucleus, where the metallicity rises by 0.3 dex compared to the nearby regions. Presently we cannot explain this feature, it may be connected to the globular cluster which might have fallen into the slit.

VCC 2050 = IC 3779 (Fig 29). Probable inclined disc is reported in this galaxy by Lisker et al. (2006). The observed velocity dispersion in this object is too low to be precisely measured. There is a significant metallicity gradient, whereas the signal is not sufficient to detect any changes in the age distribution. The luminosity-weighted age in the central part is quite young (2.5 Gyr) and we see faint emission lines in the fitting residuals.

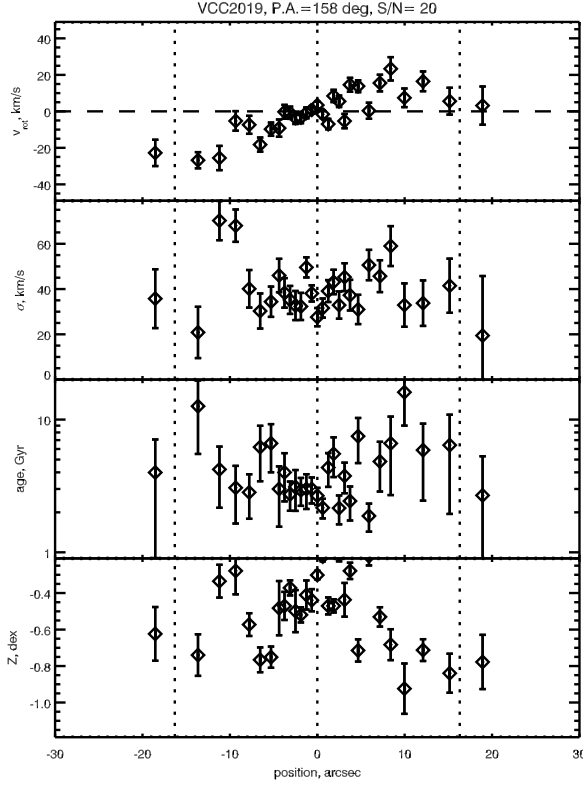


Figure 27. Kinematics and stellar populations of VCC 2019 (Palomar DSS). See Fig 4 for details.

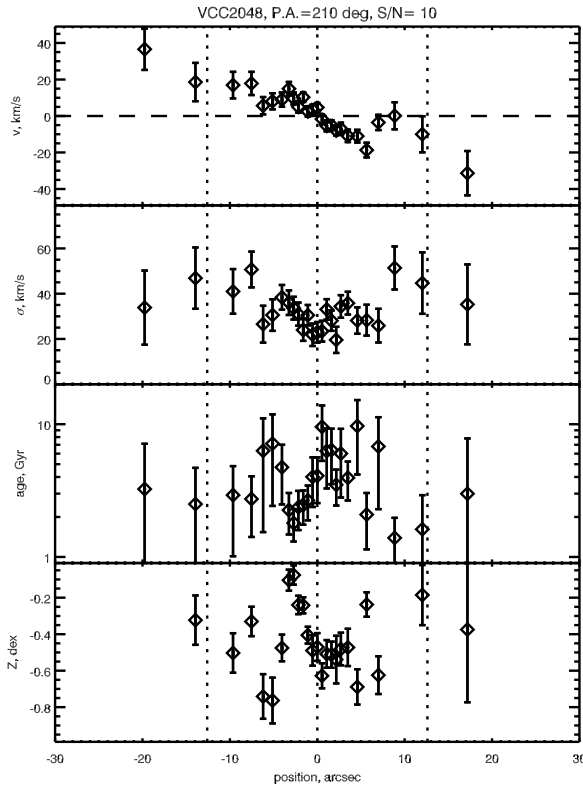


Figure 28. Kinematics and stellar populations of VCC 2048 (OHP CARELEC). See Fig 4 for details.

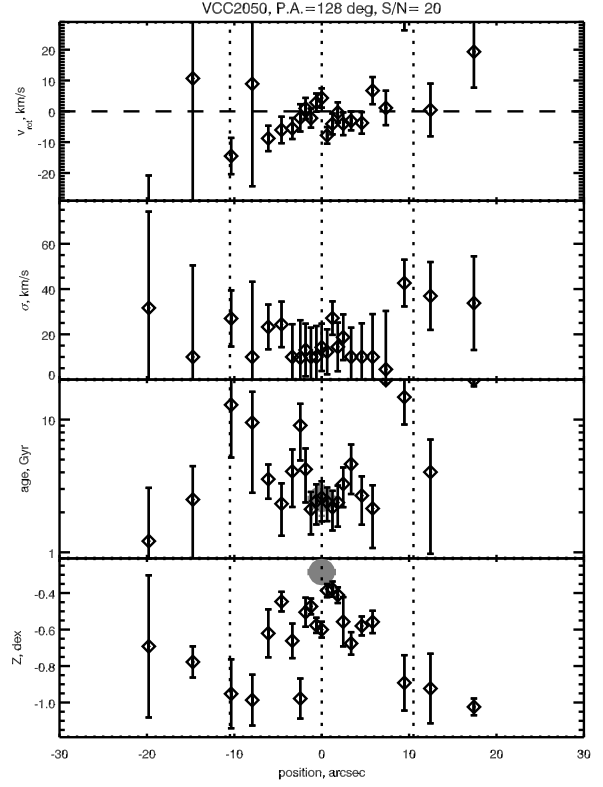


Figure 29. Kinematics and stellar populations of VCC 2050 (Palomar DSS). See Fig 4 for details.

## 5 SUMMARY AND CONCLUSIONS

We have presented the first large dataset of spectroscopically derived radial profiles of stellar population parameters for dwarf early-type galaxies made by re-analysing some of the published spectroscopic data. Thanks to the usage of the NBURSTs full spectral fitting technique we have improved the stellar kinematics compared to van Zee et al. (2004b) reaching comparable quality of measurements to those presented in Geha et al. (2002, 2003) but generally going out to  $1 r_e$  or further from the centre. We have performed the stellar population analysis of the spectra where only kinematical data were available (Simien & Prugniel 2002). Our measurements of the nuclear stellar populations are in a good agreement with the results obtained from the fitting of SDSS DR6 spectra.

Significant metallicity gradients are often observed in dE/dS0 galaxies, although in some of the objects the metallicity distribution is completely constant along the radius. There is a tendency to the dichotomy in the distribution of the metallicity gradients {metallicity profiles are either nearly flat or steeply decreasing along the radius, reaching  $>0.9 \text{ dex } r_e^{-1}$  in VCC 437. In none of the cases we see a statistically significant positive gradient. Age distribution along the radius usually exhibits flat behaviour. If any gradients in age exist, they cannot be clearly detected using the existing datasets.

Levels of  $\alpha$ -enhancement as derived from the Lick indices exhibit no statistically significant changes along the radius and between the nuclei and main discs/spheroids in all objects, but VCC 1036, where the value in the nuclear



region is nearly solar ( $[Mg/Fe] = 0.05$  dex), whereas it stays super-solar ( $+0.17$  dex) along the radius out to  $1.2 r_e$ .

Stellar populations in the nuclear regions are usually more metal-rich than in the main galactic bodies, and the central values of the luminosity-weighted metallicity are higher than what one would expect from the simple interpolation of the metallicity gradients toward the centres. A remarkable fraction of galaxies (11 or 27) demonstrate luminosity-weighted ages in the nuclear regions to be younger than those of the main galactic bodies, with the difference exceeding 7 Gyr in VCC 917 and VCC 490.

These chemically and evolutionarily decoupled nuclear regions are always associated with the drops in the velocity dispersion profiles. Only in those cases, where the velocity dispersions are too low to be measured with the present data, the  $\sigma$ -drops are not observed. In these cases, the mass-to-light ratios change significantly along the radius, pointing out to unrighteous use of constant  $M/L$  dynamical models.

In certain objects (VCC 990, 1122, 1250, 1261, 2019, and 2050) we detected faint emission lines (H $\delta$ , D III)] in the nuclear regions, associated with the chemically and evolutionarily decoupled cores.

We discovered four kinematically decoupled rotating cores in bright members of our sample (VCC 917, 1036, 1261, and 1545), two of them (VCC 917 and 1261) being hosted by the galaxies with very low if any major axis rotation. In all cases KDCs are associated with young metal-rich stellar populations and velocity dispersion drops.

Finally, we see remarkable resemblance between internal structure of dE/dS0s and of intermediate-mass and giant early-type galaxies. Some low-luminosity objects after detailed analysis look like "scaled down" versions of more luminous counterparts (e.g. VCC 917/1261 and NGC 5813, VCC 1545 and NGC 4365), suggesting possible similarities between their evolutionary paths. Some physical processes, e.g. major mergers and secular evolution, are usually considered to rule the life of giant early-type galaxies. We have to revise their applicability to explain the dE/dS0 evolution.

#### ACKNOWLEDGMENTS

Author is grateful to Liese Van Zee, who made the Palomar dE data available making this study possible. Author thanks Gary Mamon, Francoise Combes, Veronique Cayatte, Paola Di Matteo, and Olga Sil'chenko for useful discussions and suggestions and to an anonymous referee for valuable comments which helped to improve this manuscript. This project is supported by the RFBR grant 07-02-00229-a. This research has made use of SAO Image DSS9, developed by Smithsonian Astrophysical Observatory; Aadin developed by the Centre de Données Astronomiques de Strasbourg; "explore-dss" script by G. Mamon. We used the spectra provided by the HyperLeda FITS archive and by the SDSS project.

Funding for the SDSS and SDSS-II has been provided by the Alfred P. Sloan Foundation, the Participating Institutions, the National Science Foundation, the U.S. Department of Energy, the National Aeronautics and Space Administration, the Japanese Monbukagakusho, the Max Planck Society, and the Higher Education Funding Council for England. The SDSS Web Site is <http://www.sdss.org/>.

#### REFERENCES

- Abadi M. G., Moore B., Bower R. G., 1999, *MNRAS*, 308, 947
- Adelman-McCarthy J. K. et al., 2008, *ApJS*, 175, 297
- Ananiasiev V. L., Dodonov S. N., Moiseev A. V., 2001, in Ossipkov L. P., Nikiforov I. I., eds, *Stellar Dynamics: from Classic to Modern*, 103
- Barazza F. D., Binggeli B., Jerjen H., 2002, *A & A*, 391, 823
- Bender R., Nieto J.-L., 1990, *A & A*, 239, 97
- Bertola F., Capaccioli M., 1975, *ApJ*, 200, 439
- Binggeli B., Sandage A., Tammann G. A., 1985, *AJ*, 90, 1681
- Boselli A., Boissier S., Cortese L., Gavazzi G., 2008, *ApJ*, 674, 742
- Boselli A., Boissier S., Cortese L., Gavazzi G., 2008, *A & A*, 489, 1015
- Cappellari M., Copin Y., 2003, *MNRAS*, 342, 345
- Cappellari M., Emsellem E., 2004, *PASP*, 116, 138
- Chilingarian I., 2006, PhD thesis, Moscow State University, Moscow & Université Claude Bernard, Lyon, astro-ph/0611893
- Chilingarian I., Cayatte V., Bergond G., 2008a, *MNRAS*, 390, 906
- Chilingarian I., Ananiasiev V., Bonnarel F., Dodonov S., Louys M., Zolotukhin I., 2007a, in Shaw R. A., Hill F., Bell D. J., eds, *Astronomical Data Analysis Software and Systems XVI*, Vol. 376 of *Astronomical Society of the Pacific Conference Series*, 217
- Chilingarian I., Prugniel P., Sil'chenko O., Koleva M., 2007b, in Vazdekis A., R. Peletier R., eds, *Stellar Populations as Building Blocks of Galaxies* Vol. 241 of *IAU Symposium*, Cambridge University Press, Cambridge, UK, 175
- Chilingarian I., Sil'chenko O., Ananiasiev V., Prugniel P., 2008b, in Knäpen J. H., Mahoney T. J., Vazdekis A., eds, *Pathways Through an Eclectic Universe* Vol. 390 of *Astronomical Society of the Pacific Conference Series*, p. 296
- Chilingarian I. V., Cayatte V., Durret F., Adam C., Balkowski C., Chemin L., Lagana T. F., Prugniel P., 2008c, *A & A*, 486, 85
- Chilingarian I. V., Prugniel P., Sil'chenko O. K., Ananiasiev V. L., 2007c, *MNRAS*, 376, 1033
- Chilingarian I. V., Sil'chenko O. K., Ananiasiev V. L., Prugniel P., 2007d, *Astronomy Letters*, 33, 292
- Cid Fernandes R., Mateus A., Sodré L., Stasinska G., Gomes J. M., 2005, *MNRAS*, 358, 363
- Derijcke S., Dejonghe H., Zeilinger W. W., Haug K. T., 2001, *ApJ*, 559, L21
- Derijcke S., Dejonghe H., Zeilinger W. W., Haug K. T., 2003, *A & A*, 400, 119
- Derijcke S., Dejonghe H., Zeilinger W. W., Haug K. T., 2004, *A & A*, 426, 53
- Derijcke S., Michielsen D., Dejonghe H., Zeilinger W. W., Haug K. T., 2005, *A & A*, 438, 491
- Ferguson H. C., Binggeli B., 1994, *A & A Rev.*, 6, 67
- Ferrarese L., Côte P., Jordan A., Peng E. W., Blakeslee J. P., Piatek S., Mei S., Merritt D., Milosavljević M., Tonry J. L., West M. J., 2006, *ApJS*, 164, 334
- Fioc M., Rocca-Volmerange B., 1997, *A & A*, 326, 950
- Fukugita M., Shimazaki K., Ichikawa T., 1995, *PASP*, 107, 945
- Geha M., Guhathakurta P., van der Marel R. P., 2002, *AJ*,

- 124, 3073
- Geha M., Guhathakurta P., van der Marel R. P., 2003, *A J*, 126, 1794
- Geha M., Guhathakurta P., van der Marel R. P., 2005, *A J*, 129, 2617
- Graham A. W., Guzman R., 2003, *A J*, 125, 2936
- Gunn J. E. et al., 2006, *A J*, 131, 2332
- Jerjen H., Kalnajs A., Binggeli B., 2000, *A & A*, 358, 845
- Janz J., Lisker T., 2008, *ApJ*, 689, L25
- Koleva M., Bavouzet N., Chilingarian I., Prugniel P., 2007, in Kissler-Patig M., Walsh J. R., Roth M. M., eds, *Science Perspectives for 3D Spectroscopy*, 153
- Koleva M., Prugniel P., Ocvirk P., Le Borgne D., Soubiran C., 2008, *MNRAS*, 385, 1998
- Kornendy J., Fisher D. B., Comell M. E., Bender R., 2008, *Accepted to ApJS*, [arXiv:0810.1681](#)
- Kuntschner H., 2004, *A & A*, 426, 737
- Kuntschner H., Emmell E., Bacon R., Bureau M., Cappellari M., Davies R. L., de Zeeuw P. T., Falcon-Barroso J., Krajkovic D., McDermid R. M., Peletier R. F., Sarzi M., 2006, *MNRAS*, 369, 497
- Le Borgne D., Rocca-Volmerange B., Prugniel P., Lancon A., Floc M., Soubiran C., 2004, *A & A*, 425, 881
- Lisker T., Grebel E. K., Binggeli B., 2006, *A J*, 132, 497
- Lisker T., Grebel E. K., Binggeli B., 2008, *A J*, 135, 380
- Michielsen D., Koleva M., Prugniel P., Zeilinger W. W., Derijcke S., Dejonghe H., Pasquali A., Ferreras I., Debattista V. P., 2007, *ApJ*, 670, L101
- Michielsen D., Boselli A., Conselice C. J., Toloba E., Whaley I. M., Aragon-Salamanca A., Balcells M., Cardiel N., Cenarro A. J., Gorgas J., Peletier R. F., Vazdekis A., 2008, *MNRAS*, 385, 1374
- Moore B., Katz N., Lake G., Dressler A., Oemler A., 1996, *Nature*, 379, 613
- Ocvirk P., Pichon C., Lancon A., Thiebaud E., 2006, *MNRAS*, 365, 74
- Paturel G., Petit C., Prugniel P., Theureau G., Rousseau J., Brouty M., Dubois P., Cambresy L., 2003, *A & A*, 412, 45
- Pedraz S., Gorgas J., Cardiel N., Sanchez-Blazquez P., Guzman R., 2002, *MNRAS*, 332, L59
- Prugniel P., Chilingarian I., Silchenko O., Afanasiev V., 2005, in Jerjen H., Binggeli B., eds, *IAU Colloq. 198: Near-elds cosmology with dwarf elliptical galaxies*, 73
- Prugniel P., Soubiran C., Koleva M., Le Borgne D., 2007, *astro-ph/0703658*
- Rakos K., Schombert J., Maitzen H. M., Prugovecki S., Odeh A., 2001, *A J*, 121, 1974
- Salpeter E. E., 1955, *ApJ*, 121, 161
- Silchenko O., 2006, *ApJ*, 641, 229
- Simien F., Prugniel P., 2002, *A & A*, 384, 371
- Stiavelli M., Miller B. W., Ferguson H. C., Mack J., Whitmore B. C., Lotz J. M., 2001, *A J*, 121, 1385
- Thomas D., Brinoulle F., Bender R., Hopp U., Greggio L., Maraston C., Saglia R. P., 2006, *A & A*, 445, L19
- Thomas D., Maraston C., Bender R., 2003, *MNRAS*, 339, 897
- van der Marel R. P., Franx M., 1993, *ApJ*, 407, 525
- van Dokkum P. G., 2001, *PASP*, 113, 1420
- van Zee L., Barton E. J., Skillman E. D., 2004a, *A J*, 128, 2797
- van Zee L., Skillman E. D., Haynes M. P., 2004b, *A J*, 128, 121
- White S. D. M., Frenk C. S., 1991, *ApJ*, 379, 52
- Worthey G., 1994, *ApJS*, 95, 107
- Worthey G., Faber S. M., Gonzalez J. J., Burstein D., 1994, *ApJS*, 94, 687